

## Sea Ice and Cloud Processes Mediating Compensation between Atmospheric and Oceanic Meridional Heat Transports across the CMIP6 Preindustrial Control Experiment<sup>o</sup>

PRAJVALA KURTAKOTI<sup>a,b</sup>, WILBERT WEIJER,<sup>c</sup> MILENA VENEZIANI,<sup>d</sup> PHILIP J. RASCH,<sup>e,f</sup> AND TARUN VERMA<sup>g,b</sup>

<sup>a</sup> Center for Nonlinear Studies (CNLS), Los Alamos National Laboratory, Los Alamos, New Mexico

<sup>b</sup> Department of Earth and Planetary Sciences, Johns Hopkins University, Maryland

<sup>c</sup> Computational Physics and Methods (CCS-2), Los Alamos National Laboratory, Los Alamos, New Mexico

<sup>d</sup> Fluid Dynamics and Solid Mechanics (T-3), Los Alamos National Laboratory, Los Alamos, New Mexico

<sup>e</sup> Pacific Northwest National Laboratory, Richland, Washington

<sup>f</sup> Department of Atmospheric Sciences, University of Washington, Seattle, Washington

<sup>g</sup> Program in Atmospheric and Oceanic Sciences, Princeton University, Princeton, New Jersey

(Manuscript received 23 February 2023, in final form 13 September 2023, accepted 23 October 2023)

**ABSTRACT:** Bjerknes compensation (BJC) refers to the anticorrelation observed between atmospheric and oceanic heat transport (AHT/OHT) variability, particularly on decadal to longer time scales that may be important to the predictability of the climate system. This study investigates the spread in BJC across fully coupled simulations of phase 6 of the Coupled Model Intercomparison Project (CMIP6) and critical processes (particularly related to sea ice and clouds) that may contribute to that spread. BJC on decadal to longer time scales is confirmed across all the simulations evaluated, and it is strongest in the Northern Hemisphere (NH) between 60° and 70°N. At these latitudes, BJC appears to be primarily driven by the exchange of turbulent fluxes (sensible and latent) in the Greenland, Iceland, and Barents Seas. Metrics to break down how sea ice and clouds uniquely modify the radiative balance of the polar atmosphere during anomalous OHT events are presented. These metrics quantify the impacts of sea ice and clouds on surface and top of atmosphere (latent, sensible, longwave, and shortwave radiative) energy fluxes. Cloud responses tend to counter the clear sky impacts over the Marginal Ice Zone (MIZ). It is further shown that the degree of BJC present in a simulation at high latitudes is heavily influenced by the sensitivity of the sea ice to OHT, which is most influential over the MIZ. These results are qualitatively robust across models and explain the intermodel spread in NH BJC in the preindustrial control experiment.

**KEYWORDS:** Arctic; Atmosphere-ocean interaction; Feedback; Ice loss/growth; Radiative fluxes; Climate models

### 1. Introduction

Redistribution of heat from the tropics to the poles is accomplished through meridional heat transport (MHT) by the ocean and the atmosphere and plays a crucial role in modulating Earth's climate (Czaja and Marshall 2006; Farneti and Vallis 2013; Trenberth et al. 2019). The factors responsible for changes in the MHT in response to greenhouse gases and other anthropogenic forcing are not well understood, making climate predictions of the future Arctic and the adjoining midlatitude regions uncertain. A large part of this uncertainty results from the lack of complete understanding of various ocean and sea ice processes influencing heat transport and how they change in a warmer climate (Oldenburg et al. 2018; Notz and SIMIP Community 2020; Hankel and Tziperman 2021). To properly quantify the effects of

the planet's recent warming on the polar ocean and atmosphere, one must understand the climate system's natural variability, including the physical mechanisms and feedbacks that modulate it.

Attributing contributions from the ocean and the atmosphere to MHT is necessary while trying to disentangle responses that arise from natural variability from those due to anthropogenic effects. On decadal to longer time scales, Bjerknes compensation (BJC) enables variations in the atmospheric and oceanic heat transport to balance each other, assuming that the fluxes at the top of the atmosphere (TOA) and ocean heat content remain approximately constant (Bjerknes 1964). Compensation between the ocean and atmosphere is crucial for a stable MHT in the climate system (Yang et al. 2015). BJC further facilitates the radiative fluxes at the TOA to remain stable, playing a crucial role in maintaining the energy balance and providing insights into the predictability of the climate system on decadal to longer time scales (Shi and Yang 2021; Outten et al. 2018). BJC in the Northern Hemisphere (NH), quantified as anticorrelation between decadal anomalies of atmospheric heat transport (AHT) and ocean heat transport (OHT), has been observed in fully coupled climate models (Outten et al. 2018;

<sup>o</sup> Denotes content that is immediately available upon publication as open access.

<sup>o</sup> Supplemental information related to this paper is available at the Journals Online website: <https://doi.org/10.1175/JCLI-D-23-0103.s1>.

Corresponding author: Prajvala Kurtakoti, prajvala.kurtakoti@gmail.com

Dai et al. 2017; van der Swaluw et al. 2007; Shaffrey and Sutton 2006) as well as reanalysis datasets (Liu et al. 2020).

Studies using fully coupled climate models have found that BJC on decadal to longer time scales occurs in the NH subpolar region (between 50° and 80°N; van der Swaluw et al. 2007), with highest compensation near 70°N (Shaffrey and Sutton 2006; van der Swaluw et al. 2007; Outten et al. 2018; Liu et al. 2020) and no significant compensation in the Southern Ocean. Shaffrey and Sutton (2006) show that the decadal variability of OHT can be entirely explained by the Atlantic Ocean component of OHT, which they attribute to variations in the strength of the Atlantic meridional overturning circulation. Results from van der Swaluw et al. (2007) agree with this finding, and additionally show that the highest compensation occurs at 70°N when the ocean leads the atmosphere by one year, suggesting that the ocean forces the atmosphere on decadal time scales. Outten et al. (2018) investigate BJC across fully coupled simulations in the Coupled Model Intercomparison Project phase 5 (CMIP5) preindustrial and historical experiments. Their study identifies BJC in the subpolar regions of all the analyzed simulations and finds that some models also exhibit BJC in the midlatitudes, which they attribute to the presence of storms driving strong air-sea interactions. Anthropogenic warming can complicate these interactions by introducing additional forcings to TOA and surface fluxes (von Schuckmann et al. 2016) and changing ocean heat content (Cheng et al. 2022). Thus, BJC changes in response to global warming are not known.

The present study explores the variability of BJC under the influence of internal variability (i.e., without the effect of anthropogenic forcing). Our primary objective is to investigate the factors that influence BJC natural variability and, in particular, the role of sea ice and clouds in mediating energy transports in the ocean and atmosphere. We believe that our findings will give perspective as well as still be relevant to the understanding of the magnitude and role of BJC in the context of global warming.

Sea ice and its effects on the polar atmosphere and ocean are expected to change dramatically in a warmer climate. The surface albedo feedback represents first-order positive feedback where sea ice is present (Budyko 1969; Hall 2004; Goosse et al. 2018). While climate feedbacks are important in the context of a warming Arctic, they also operate in polar regions under natural internal variability. Radiative feedbacks associated with clouds, temperature, and water vapor also play essential roles in polar regions (Pithan and Mauritsen 2014). The influence of clouds on the radiative energy budget is essential for regulating both the shortwave and longwave radiative fluxes at the surface and at the TOA (Ramanathan et al. 1989). Cloud representation in CMIP6 models is essential not only because they have a significant effect on Earth's radiation budget but also because cloud-climate feedbacks are a big influence on climate sensitivity (Zelinka et al. 2020).

The magnitude of the opposing net effects of shortwave cooling and longwave warming over regions covered in sea ice is more challenging to estimate due to the numerous interconnected mechanisms (involving ocean, atmosphere, cloud, sea ice, and ice sheet) through which interactions can occur (Goosse et al. 2018). In polar regions, clouds influence the

atmosphere through distinct feedbacks such as the cloud-sea ice feedback (Schweiger et al. 2008) and the cloud-optical depth feedback (Mitchell et al. 1989). Observations recently have shown that clouds can dampen the radiative impacts of Arctic sea ice loss (Alkama et al. 2020) as they increase the surface albedo over snow/sea ice compared to cloudless conditions (Stapf et al. 2020). Lauer et al. (2023) find that there is 20% less liquid water path (LWP) in CMIP6 than in CMIP5 models, and CMIP6 compares better with observations. The total water path (TWP) and cloud fraction are better represented in CMIP6 than in CMIP5 models. However, there is a large intermodel spread in the seasonal cycle of TWP and cloud fraction, which points to the consequences of different cloud parameterization schemes used in different models (Wei et al. 2021).

The natural variability in OHT in fully coupled GCMs is linked to fluctuations in Arctic temperature on decadal time scales (Aylmer et al. 2022), which diminish in a warmer climate without sea ice (Reusen et al. 2019). Observations indicate that mechanisms leading to the Arctic becoming sea ice-free involve a positive feedback between sea ice and low-level clouds that accelerate its warming (Philipp et al. 2020). Studies using fully coupled GCMs have further shown the importance of atmospheric feedbacks in abrupt sea ice loss seen in warming scenarios (Hankel and Tziperman 2021). In this study, we closely examine the role of sea ice and cloud in modulating BJC through surface and TOA radiative fluxes.

This paper is organized as follows. Section 2 describes our methodology, including the CMIP6 model experiments, the computation of AHT and its components, and the calculations needed to separate cloud from clear-sky radiation effects. Main results are presented in section 3 and discussed in section 4. A summary and conclusions are included in section 5.

## 2. Data and methods

### a. The CMIP6 models

The CMIP6 simulations used in this study are listed in Table 1, along with their names, the modeling centers that performed them, their version and member numbers, and their total length in the number of simulated years. We selected 18 preindustrial control (piControl) simulations (available as of August 2023) that provided the necessary monthly model output variables to compute the OHT and AHT and are of comparable spatial resolution.

### b. Ocean and atmospheric heat transport

The OHT is given by the CMIP6 variable "hfbasin", which is the northward oceanic heat transport as a function of latitude, zonally integrated around the globe. The AHT is calculated using the methodology first described for climate models in Magnusdottir and Saravanan (1999) and further discussed in Shaffrey and Sutton (2006) and van der Swaluw et al. (2007). Specifically, our approach assumes that energy storage in the atmosphere is negligible on decadal time scales, and that meridional heat transport balances the divergence of fluxes at the surface and the TOA. AHT can therefore be estimated by meridionally integrating the zonally integrated net

TABLE 1. List of CMIP6 models used in this study, along with the respective institution that ran these simulations. The length in years of the preindustrial run along with the member, version, key reference, and the data citations are also given.

Institution	Model	Reference	Data	Member	Version	Length (years)
CNRM-CERFACS	CNRM-ESM2-1	Séférian et al. (2019)	Séférian (2018)	r1i1p1f1	v20181115	500
CNRM-CERFACS	CNRM-CM6-1	Voldoire et al. (2019)	Voldoire (2018)	r1i1p1f1	v20180814	500
EC-Earth-Consortium	EC-Earth3	Dööscher et al. (2022)	EC-Earth (2019a)	r1i1p1f1	v20200312	501
EC-Earth-Consortium	EC-Earth3-Veg	Dööscher et al. (2022)	EC-Earth (2019b)	r1i1p1f1	v20200919	500
IPSL	IPSL-CM6A-LR	Servonnat et al. (2020)	Boucher et al. (2018)	r1i1p1f1	v20181123	1200
NASA-GISS	GISS-E2-1-G	Kelley et al. (2020)	NASA-GISS (2018)	r1i1p1f1	v20180824	851
MRI	MRI-ESM2-0	Yukimoto et al. (2019b)	Yukimoto et al. (2019a)	r1i1p1f1	v20190222	701
CCCma	CANESM5	Swart et al. (2019d)	Swart et al. (2019b)	r1i1p1f1	v20190429	1000
CCCma	CANESM5.1	Swart et al. (2019d)	Swart et al. (2019c)	r1i1p1f1	v20190429	501
CCCma	CANESM5-CanOE	Christian et al. (2022)	Swart et al. (2019a)	r1i1p2f1	v20190429	501
NCC	NorESM2-LM	Seland et al. (2020)	Seland et al. (2019)	r1i1p1f1	v20210118	501
HAMMOZ-Consortium	MPI-ESM1-2-HAM	Mauritzen et al. (2019)	Neubauer et al. (2019)	r1i1p1f1	v20200120	1000
MOHC	UKESM1-0-LL	Sellar et al. (2019)	Tang et al. (2019)	r1i1p1f1	v20200828	1880
MOHC	HadGEM3-GC31-LL	Kuhlbrodt et al. (2018)	Ridley et al. (2018)	r1i1p1f1	v20190628	500
MOHC	HadGEM3-GC31-MM	Williams et al. (2018)	Ridley et al. (2019)	r1i1p1f1	v20190920	500
SNU	SAM0-UNICON	Park et al. (2019)	Park and Shin (2019)	r1i1p1f1	v20190910	700
CMCC	CMCC-CM2-SR5	Cherchi et al. (2019)	Lovato and Peano (2020)	r1i1p1f1	v20200616	501
NOAA-GFDL	GFDL-CM4	Held et al. (2019)	Guo et al. (2018)	r1i1p1f1	v20180701	500

heat flux into the atmosphere column, which is given by the net flux at the surface ( $F_{\text{sfc}}^{\text{net}}$ ) minus the net flux at the TOA ( $F_{\text{TOA}}^{\text{net}}$ ):

$$\text{AHT}(\Phi) = \int_{90^{\circ}\text{S}}^{\Phi} \left\{ \int_0^{2\pi} [F_{\text{sfc}}^{\text{net}}(\phi, \lambda) - F_{\text{TOA}}^{\text{net}}(\phi, \lambda)] a d\lambda \right\} a \cos(\phi) d\phi, \quad (1)$$

where  $a$  is Earth's radius,  $\phi$  is latitude,  $\Phi$  is the specific latitude where AHT is integrated to,  $\lambda$  is longitude, and

$$F_{\text{sfc}}^{\text{net}} = \text{LW}_{\text{sfc}} + \text{SW}_{\text{sfc}} + \text{LHF}_{\text{sfc}} + \text{SHF}_{\text{sfc}},$$

$$F_{\text{TOA}}^{\text{net}} = \text{LW}_{\text{TOA}} + \text{SW}_{\text{TOA}}.$$

Above, we have introduced the following formalism:  $\text{LW}_{\text{sfc}}$  = net longwave radiation at the surface;  $\text{SW}_{\text{sfc}}$  = net shortwave radiation at the surface;  $\text{LHF}_{\text{sfc}}$  = latent heat flux at the surface;  $\text{SHF}_{\text{sfc}}$  = sensible heat flux at the surface;  $\text{LW}_{\text{TOA}}$  = outgoing longwave radiation at the TOA; and  $\text{SW}_{\text{TOA}}$  = net shortwave radiation at the TOA.

While AHT should integrate to zero from either pole to the other for the coupled system, minor numerical and physical inconsistencies in model components can introduce perceptible departures that accumulate as the integration is performed. To minimize such accumulation of errors, and considering our focus on the Northern Hemisphere, we have chosen to perform the integration from the North Pole southward. Therefore, Eq. (1) becomes

$$\begin{aligned} \text{AHT}(\Phi) = & - \int_{90^{\circ}\text{N}}^{\Phi} \int_0^{2\pi} (\text{LW}_{\text{sfc}} + \text{SW}_{\text{sfc}} + \text{LHF}_{\text{sfc}} + \text{SHF}_{\text{sfc}} \\ & - \text{LW}_{\text{TOA}} - \text{SW}_{\text{TOA}}) a^2 d\lambda \cos(\phi) d\phi. \end{aligned} \quad (2)$$

Refactoring Eq. (2) using CMIP6-specific variable names (described in Table 2) and adding labels to facilitate discussions of terms participating in the heat budget of the Arctic:

$$\begin{aligned} \text{AHT}_{\Phi_{\text{max}}} = & \int_{90^{\circ}\text{N}}^{\Phi_{\text{max}}} \left[ \begin{array}{c} \overbrace{\text{SW}_{\text{TOTAL}}}^{\text{SW}_{\text{TOA}} \text{ and } \text{SW}_{\text{sfc}}} \\ \overbrace{(\text{RSUT} - \text{RSDT}) + (\text{RSDS} - \text{RSUS})}^{\text{RLUT}} \end{array} \right. \\ & + \overbrace{\text{RLDS} - \text{RLUS}}^{\text{LW}_{\text{TOTAL}} \text{ and } \text{LW}_{\text{sfc}}} \\ & \left. \begin{array}{c} \overbrace{- \text{HFLS} - \text{HFSS}}^{\text{LHF}_{\text{sfc}} \text{ and } \text{SHF}_{\text{sfc}}} \\ \text{TURB}_{\text{TOTAL}} \end{array} \right] dA, \end{aligned} \quad (3)$$

where  $dA$  is used in place of  $a^2 \cos(\phi) d\lambda d\phi$  to represent the local cell area.

### c. Separating cloud and clear-sky contributions

To explore the role of clouds and sea ice in more detail we will further break down the radiative fluxes in cloud and clear-sky contributions. All-sky TOA, surface, and net fluxes are given by

$$\begin{aligned} F_{\text{all-sky}}^{\text{TOA}} &= \text{RSDT} - \text{RSUT} - \text{RLUT} \\ &= [\text{downward (incident)} - \text{upward (outgoing)}] \\ &\quad \times \text{SW at TOA} - [\text{upward} \text{ LW at TOA}], \end{aligned}$$

$$\begin{aligned} F_{\text{all-sky}}^{\text{sfc}} &= \text{RSUS} - \text{RSDS} + \text{RLUS} - \text{RLDS} \\ &= [\text{upward} - \text{downward}] \text{ SW at surface} \\ &\quad + [\text{upward} - \text{downward}] \text{ LW at surface}, \end{aligned}$$

$$F_{\text{all-sky}}^{\text{net}} = F_{\text{all-sky}}^{\text{TOA}} + F_{\text{all-sky}}^{\text{sfc}}.$$

TABLE 2. List of CMIP6 variables used in this study, along with the CMIP6 table under which it can be found. The variable long name, detailed description, and units are also given.

CMIP6 variable name	CMIP6 table	Variable long name	Description	Units
HFBASIN	OMON	Northward ocean heat transport	Contains contributions from physical processes affecting the northward heat transport, including resolved advection, parameterized advection, lateral diffusion, etc; a function of latitude and basin	W
RSDT	AMON	TOA incident shortwave radiation	Shortwave radiation incident at the top of the atmosphere	$\text{W m}^{-2}$
RSUS	AMON	Surface upwelling shortwave radiation	“Surface” means the lower boundary of the atmosphere; “shortwave” means shortwave radiation; upwelling radiation is radiation from below, not “net upward”; when thought of as being incident on a surface, a radiative flux is sometimes called “irradiance”	$\text{W m}^{-2}$
RSUT	AMON	TOA outgoing shortwave radiation	Outgoing shortwave radiation at the top of the atmosphere	$\text{W m}^{-2}$
RSUTCS	AMON	TOA outgoing clear-sky shortwave radiation	Outgoing shortwave radiation at the top of the atmosphere calculated in the absence of clouds	$\text{W m}^{-2}$
RLUT	AMON	TOA outgoing longwave radiation	Outgoing longwave radiation at the top of the atmosphere	$\text{W m}^{-2}$
RLUTCS	AMON	TOA outgoing clear-sky longwave radiation	Upwelling clear-sky longwave radiation at top of atmosphere	$\text{W m}^{-2}$
RLDS	AMON	Surface downwelling longwave radiation	“Surface” means the lower boundary of the atmosphere; “longwave” means longwave radiation; downwelling radiation is radiation from above, not the same as “net downward”	$\text{W m}^{-2}$
RLDSCS	AMON	Surface downwelling clear-sky longwave radiation	Surface downwelling clear-sky longwave radiation	$\text{W m}^{-2}$
RSDS	AMON	Surface downwelling shortwave radiation	Surface solar irradiance	$\text{W m}^{-2}$
RSDSCS	AMON	Surface downwelling clear-sky shortwave radiation	Surface solar irradiance clear sky	$\text{W m}^{-2}$
RSUSCS	AMON	Surface upwelling clear-sky shortwave radiation	Surface upwelling clear-sky shortwave radiation	$\text{W m}^{-2}$
RLUS (all-sky/ clear-sky)	AMON	Surface upwelling longwave radiation	“Surface” means the lower boundary of the atmosphere; “longwave” means longwave radiation; upwelling radiation is radiation from below, not the same as net upward	$\text{W m}^{-2}$
LHF/HFLS	AMON	Surface upward latent heat flux	Surface latent heat flux is the exchange of heat between the surface and the air due to evaporation	$\text{W m}^{-2}$
SHF/HFSS	AMON	Surface upward sensible heat flux	Surface sensible heat flux is the exchange of heat between the surface and the air by motion of air	$\text{W m}^{-2}$
CLWVI	AMON	Condensed water path	Mass of condensed (liquid + ice) water in the column divided by the area of the column (not just the area of the cloudy portion of the column)	$\text{kg m}^{-2}$
CLIVI	AMON	Ice water path	Mass of ice water in the column divided by the area of the column (not just the area of the cloudy portion of the column)	$\text{kg m}^{-2}$

Corresponding clear-sky fluxes are

$$\begin{aligned} F_{\text{clear-sky}}^{\text{TOA}} &= \text{RSDT} - \text{RSUTCS} - \text{RLUTCS} \\ &= [\text{downward (incident)} \\ &\quad - \text{clear-sky upward (outgoing)] SW at TOA} \\ &\quad - [\text{clear-sky upward}] \text{ LW}_{\text{TOA}}, \end{aligned}$$

$$\begin{aligned} F_{\text{clear-sky}}^{\text{sfc}} &= \text{RSUSCS} - \text{RSDSCS} + \text{RLUS} - \text{RLDSCS} \\ &= [\text{clear-sky upward} - \text{clear-sky downward}] \\ &\quad \times \text{SW at surface} + [\text{upward} \\ &\quad - \text{clear-sky downward}] \text{ LW at surface}, \end{aligned}$$

$$F_{\text{clear-sky}}^{\text{net}} = F_{\text{clear-sky}}^{\text{TOA}} + F_{\text{clear-sky}}^{\text{sfc}}.$$

And net fluxes due to clouds alone are then given by

$$F_{\text{clouds}}^{\text{net}} = F_{\text{all-sky}}^{\text{net}} - F_{\text{clear-sky}}^{\text{net}},$$

with separating contributions due to shortwave and longwave fluxes given by the following terms (using the variable names introduced above):

$$\begin{aligned} \text{SW}_{\text{clouds}}^{\text{net}} &= \text{RSUS} - \text{RSUSCS} - \text{RSDS} + \text{RSDSCS} - \text{RSUT} \\ &\quad + \text{RSUTCS}, \end{aligned}$$

$$\text{LW}_{\text{clouds}}^{\text{net}} = -\text{RLUT} + \text{RLUTCS} - \text{RLDS} + \text{RLDSCS}.$$

Reconstructing  $F_{\text{all-sky}}^{\text{net}}$  again as the sum of  $F_{\text{clouds}}^{\text{net}}$  and  $F_{\text{clear-sky}}^{\text{net}}$ ,

$$\text{LW}_{\text{all-sky}}^{\text{net}} = \underbrace{[\text{RLUS} - \text{RLDSCS}]}_{\text{LW}_{\text{clouds}}^{\text{sfc}}} + \underbrace{[-\text{RLUTCS}]}_{\text{LW}_{\text{clouds}}^{\text{TOA}}} \\ + \underbrace{[-\text{RLDS} + \text{RLDSCS}]}_{\text{LW}_{\text{clouds}}^{\text{sfc}}} + \underbrace{[-\text{RLUT} + \text{RLUTCS}]}_{\text{LW}_{\text{clouds}}^{\text{TOA}}} \quad (4)$$

$$\text{SW}_{\text{all-sky}}^{\text{net}} = \underbrace{[\text{RSUSCS} - \text{RSDSCS}]}_{\text{SW}_{\text{clouds}}^{\text{sfc}}} + \underbrace{[\text{RSDT} - \text{RSUTCS}]}_{\text{SW}_{\text{clouds}}^{\text{TOA}}} \\ + \underbrace{[\text{RSUS} - \text{RSUSCS} - \text{RSDS} + \text{RSDSCS}]}_{\text{SW}_{\text{clouds}}^{\text{sfc}}} \\ + \underbrace{[-\text{RSUT} + \text{RSUTCS}]}_{\text{SW}_{\text{clouds}}^{\text{TOA}}} \cdot \quad (5)$$

Throughout this paper, we apply a 10-yr running mean to the detrended oceanic and atmospheric anomaly fields to focus on decadal to longer time scale variability.

### 3. Results

The presentation of the results is organized as follows. First, the piControl CMIP6 simulations are assessed in terms of their time-mean zonal-mean OHT and AHT distributions ([section 3a](#)) and their degree of BJC, quantified by the correlation between the OHT and AHT time series, as well as a quantity (defined below) known as the BJC rate, at each latitude ([section 3b](#)). We then consider the TOA and surface energy fluxes that contribute to the AHT at the latitude of maximum anticorrelation (hereafter referred to as  $\Phi_{\max}$ ), which typically falls between  $60^\circ$  and  $70^\circ\text{N}$ . Specifically, we compute the BJC rate between  $\text{OHT}_{\Phi_{\max}}$  and each AHT subcomponent in a spatially integrated sense, with the purpose of identifying the processes that contribute to NH BJC across the different piControl CMIP6 simulations ([section 3c](#)).

Third, we switch our focus to the simulation with the highest NH BJC and compute regression maps between OHT at  $65^\circ\text{N}$  (hereafter referred to as  $\text{OHT}_{65^\circ\text{N}}$ ) and each of the AHT subcomponents. We make the decision to focus on this latitude because  $65^\circ\text{N}$  is an important gateway for poleward ocean heat transport into the Nordic seas and eventually the Arctic Ocean. In addition, a fixed latitude enables a consistent comparison of the spatial response of the Arctic and subarctic to poleward OHT across different CMIP6 simulations. The regression maps allow a better visualization and quantification of the processes that drive and modulate the equatorward AHT response to an anomalous poleward  $\text{OHT}_{65^\circ\text{N}}$  and ultimately determine a high level of BJC at these northern latitudes ([section 3d](#)). Finally, we present a radiative contribution breakdown to investigate how sea ice and clouds uniquely modify the radiative budget of the polar atmosphere at the surface and TOA, and we also illustrate the response of low- and high-level clouds to anomalous poleward OHT ([sections 3e](#) and [3f](#)).

#### a. Evaluating OHT and AHT mean state

The OHT and AHT averaged over the entire time series for each CMIP6 simulation as a function of latitude are shown

in [Fig. 1](#). The multimodel means are also indicated as dashed black curves. They compare well with atmospheric and oceanic heat transports from observation-based estimates shown in [Trenberth et al. \(2019\)](#). The AHT ([Fig. 1a](#)) multimodel mean reaches maximum meridional heat transports at around  $40^\circ\text{N}$  and  $40^\circ\text{S}$ , with the value at  $40^\circ\text{S}$  being slightly larger than the value at  $40^\circ\text{N}$ , consistent with [Trenberth and Caron \(2001, their Fig. 7\)](#). The OHT ([Fig. 1b](#)) multimodel mean reaches maximum meridional heat transports at  $15^\circ\text{N}$  and  $15^\circ\text{S}$ , with the maximum at  $15^\circ\text{N}$  being  $\sim 0.5$  PW larger than the maximum at  $15^\circ\text{S}$ , also consistent with [Trenberth and Caron \(2001, their Fig. 7\)](#). Although most of the models have a realistic OHT in the Northern Hemisphere, it is worth noting that in the Southern Hemisphere five piControl simulations (IPSL:IPSL-CM6A-LR, EC-Earth-Consortium:EC-Earth3-Veg, EC-Earth-Consortium:EC-Earth3, CNRM-CERFACS:CNRM-ESM2-1, and CNRM-CERFACS:CNRM-CM6-1) show anomalous northward OHT around  $45^\circ\text{S}$ , in contrast to observationally based estimates.

#### b. Evaluation of the BJC

BJC is often defined using two quantities: the correlation between OHT and AHT time series and/or the BJC rate (discussed below). Here, we consider both definitions and show the correlation between OHT and AHT anomalies at a given latitude in [Fig. 2a](#) and similarly, the BJC rate in [Fig. 2b](#). The anomalies were calculated by removing the trend over the full time series and applying a 10-yr running mean. Additionally, the AHT and OHT anomalies were regressed onto a common grid using a linear interpolation scheme. Since some of the simulations are as long as 1800 years and the focus of this study is on multidecadal variability, we calculate the OHT–AHT correlation at all latitudes in time segments of 150 years. These correlations are then composited over the different time segments per simulation to produce [Figs. 2a](#) and [2b](#).

We find that on decadal to longer time scales, all the CMIP6 piControl simulations confirm the presence of BJC in the NH high latitudes. The multimodel mean (dashed line in [Fig. 2a](#)) shows that the most robust and consistent BJC signature is found in the NH high latitudes where OHT and AHT have the maximum tendency to compensate one another, with anticorrelations ranging between  $-0.5$  and  $-0.95$  north of  $65^\circ\text{N}$ . While the multimodel mean shows that on decadal to longer time scales, the latitude range of maximum compensation (anticorrelation greater than  $-0.7$ ) lies between  $60^\circ$  and  $70^\circ\text{N}$ , significant compensation is still occurring even at northern midlatitudes (anticorrelation over  $-0.5$ ). There is a very wide spread of values in the Southern Hemisphere, probably because there is very little decadal variability in the OHT indicating that local circulation features strongly control heat transport in some models, while others experience heat transport that is global in nature.

We further quantify BJC using the BJC rate,  $C_R$ , as defined by [Zhao et al. \(2016\)](#); specifically,

$$C_R = \Gamma(\text{OHT}, \text{AHT}) \frac{\sigma_{\text{AHT}}}{\sigma_{\text{OHT}}}, \quad (6)$$

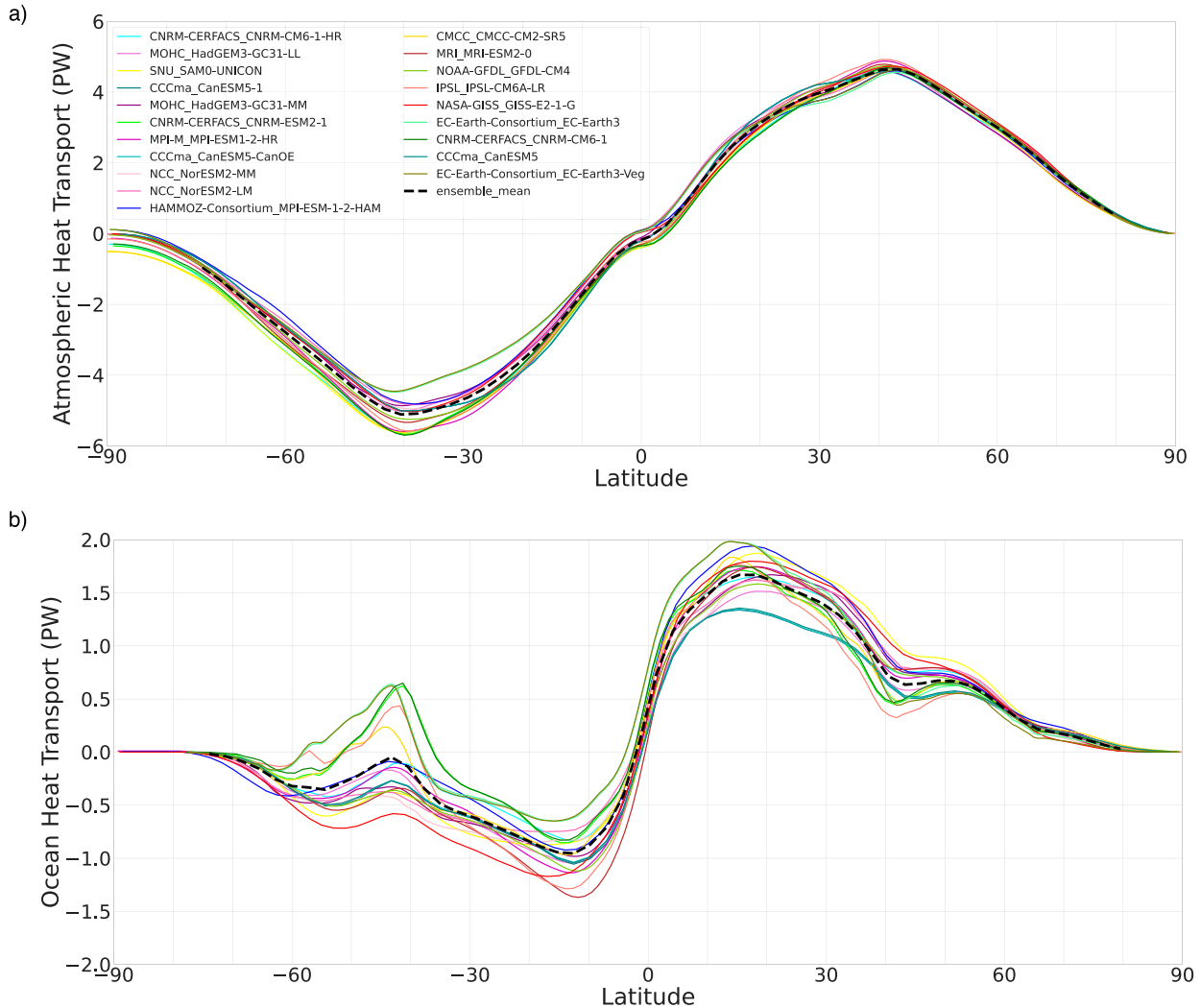


FIG. 1. Climatologies of (a) AHT and (b) OHT computed and averaged over the full time series for each CMIP6 piControl simulation. The dashed black lines represent the ensemble means.

where  $\Gamma$  is the correlation operator between AHT and OHT and  $\sigma_{\text{AHT}}$  and  $\sigma_{\text{OHT}}$  are the standard deviations of AHT and OHT at each latitude, respectively. The BJC rate is an improvement over correlation alone because it takes into account the amplitude of the AHT and OHT anomalies. While a significant negative correlation confirms the presence of compensation, the magnitude of the BJC rate ( $|C_R|$ ) also illustrates the type of compensation in the climate system. A value of  $|C_R| < 1$  indicates a climate system experiencing undercompensation (the compensating AHT is smaller than the perturbation OHT), which also means that it has negative climate feedback (Yang et al. 2016);  $|C_R| = 1$  indicates a climate system in perfect compensation (compensating AHT is equal to the perturbation OHT), which indicates the absence of a climate feedback. Finally,  $|C_R| > 1$  indicates overcompensation in the climate system (compensating AHT larger than the perturbation OHT) and a positive climate feedback. Our analysis

in Fig. 2b shows a wide range of BJC rates in NH high latitudes on decadal to longer time scales. In a stable climate local climate feedback is generally negative, and thus, the CMIP6 piControl simulations in Fig. 2b mostly exhibit undercompensation in the NH high latitudes. The magnitude of the OHT/AHT variations at 65°N is  $\approx \pm 0.1$  PW [the climatological mean of OHT and AHT at 65°N is  $\approx 0.25$  and  $\approx 2$  PW respectively (refer to Fig. 1)]. We also provide a table of BJC maximum anticorrelation and BJC rate at that latitude in Table 3. Table 3 shows that the magnitude of BJC rate at the latitude of maximum anticorrelation in the NH is not insignificant.

#### c. Regression breakdown into contribution from AHT subcomponents

To understand which processes cause AHT to be anticorrelated with OHT we break down the contribution to AHT

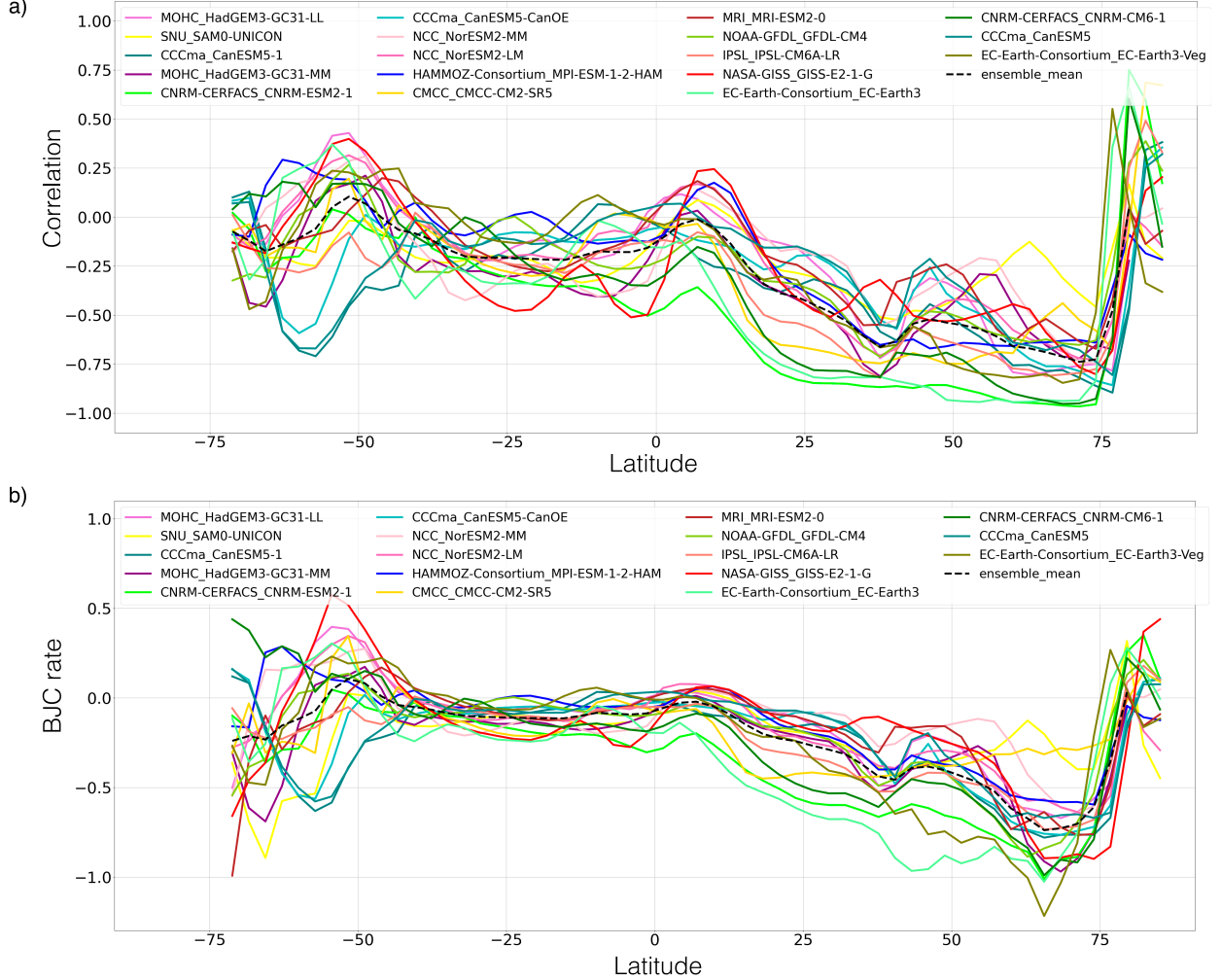


FIG. 2. (a) Correlation between OHT and AHT as a function of latitude for each CMIP6 piControl simulation. (b) BJC rate between OHT and AHT as a function of latitude for each CMIP6 piControl simulation. The dashed black line in each plot represents the ensemble mean.

from each of the energy fluxes (or AHT subcomponents) in Eq. (3) and estimate their contribution to the correlation between OHT and AHT at the latitude of maximum NH BJC (hereafter referred to as AHT/OHT<sub>Φ<sub>max</sub></sub>). We ensure that the sum of the correlations between OHT and the AHT subcomponents match the total OHT – AHT correlation as follows. Let  $A, B, C$ , and  $D$  be four time series, with  $A = B + C$ , and  $\Gamma$  be the correlation operator; then algebraic manipulation shows that

$$\Gamma(D, A) = \Gamma(D, B) \frac{\sigma_B}{\sigma_A} + \Gamma(D, C) \frac{\sigma_C}{\sigma_A}, \quad (7)$$

where the  $\sigma$  symbols represent the standard deviations of each time series, and, for example,  $\Gamma(D, B)(\sigma_B/\sigma_A)$  is the correlation between  $D$  and  $B$  weighted by  $B$ 's relative contribution to  $A$ 's variability. Using Eqs. (3) and (7) together, we obtain

$$\begin{aligned} & \Gamma(\text{OHT}_{\Phi_{\max}}, \text{AHT}_{\Phi_{\max}}) \\ &= \Gamma[\text{OHT}_{\Phi_{\max}}, (\text{SW}_{\text{TOA}} + \text{SW}_{\text{sfc}} + \text{LW}_{\text{TOA}} + \text{LW}_{\text{sfc}} + \text{LHF}_{\text{sfc}} \\ &+ \text{SHF}_{\text{sfc}})] \\ &= \Gamma(\text{OHT}_{\Phi_{\max}}, \text{SW}_{\text{TOA}}) \times \frac{\sigma_{\text{SW}_{\text{TOA}}}}{\sigma_{\text{AHT}_{\Phi_{\max}}}} + \Gamma(\text{OHT}_{\Phi_{\max}}, \text{SW}_{\text{sfc}}) \\ &\quad \times \frac{\sigma_{\text{SW}_{\text{sfc}}}}{\sigma_{\text{AHT}_{\Phi_{\max}}}} + \Gamma(\text{OHT}_{\Phi_{\max}}, \text{LW}_{\text{TOA}}) \times \frac{\sigma_{\text{LW}_{\text{TOA}}}}{\sigma_{\text{AHT}_{\Phi_{\max}}}} \\ &\quad + \Gamma(\text{OHT}_{\Phi_{\max}}, \text{LW}_{\text{sfc}}) \times \frac{\sigma_{\text{LW}_{\text{sfc}}}}{\sigma_{\text{AHT}_{\Phi_{\max}}}} + \Gamma(\text{OHT}_{\Phi_{\max}}, \text{LHF}_{\text{sfc}}) \\ &\quad \times \frac{\sigma_{\text{LHF}_{\text{sfc}}}}{\sigma_{\text{AHT}_{\Phi_{\max}}}} + \Gamma(\text{OHT}_{\Phi_{\max}}, \text{SHF}_{\text{sfc}}) \times \frac{\sigma_{\text{SHF}_{\text{sfc}}}}{\sigma_{\text{AHT}_{\Phi_{\max}}}}. \end{aligned} \quad (8)$$

TABLE 3. CMIP6 models used in this study, along with the maximum anticorrelation  $\Gamma_{\max}$  and the BJC rate  $C_R$  at the latitude  $\Phi_{\Gamma_{\max}}$  for each simulation.

CMIP6 simulation	$\Gamma$	$C_R$
CNRM-CERFACS_CNRM-ESM2-1	-0.96	-0.91
CNRM-CERFACS_CNRM-CM6-1	-0.95	-0.93
EC-Earth-Consortium_EC-Earth3	-0.94	-0.92
EC-Earth-Consortium_EC-Earth3-Veg	-0.85	-0.99
IPSL_IPSL-CM6A-LR	-0.82	-0.75
MOHC_UKESM1-0-LL	-0.81	-0.75
MOHC_HadGEM3-GC31-LL	-0.80	-0.61
CCCma_CanESM5-1	-0.78	-0.78
CCCma_CanESM5-CanOE	-0.76	-0.76
MOHC_HadGEM3-GC31-MM	-0.72	-0.95
NCC_NorESM2-MM	-0.70	-0.64
NASA-GISS_GISS-E2-1-G	-0.70	-0.89
NCC_NorESM2-LM	-0.69	-0.61
CCCma_CanESM5	-0.68	-0.67
NOAA-GFDL_GFDL-CM4	-0.66	-0.79
HAMMOZ-Consortium_MPI-ESM-1-2-HAM	-0.65	-0.56
CMCC_CMCC-CM2-SR5	-0.63	-0.29
MRI_MRI-ESM2-0	-0.62	-0.73
SNU_SAM0-UNICON	-0.34	-0.36

Combining Eqs. (8) and (6), we get

$$\begin{aligned}
 C_{R_{\Phi_{\max}}} &= \Gamma(OHT_{\Phi_{\max}}, AHT_{\Phi_{\max}}) \frac{\sigma_{AHT_{\Phi_{\max}}}}{\sigma_{OHT_{\Phi_{\max}}}} \\
 &= \left[ \Gamma(OHT_{\Phi_{\max}}, SW_{TOA}) \times \frac{\sigma_{SW_{TOA}}}{\sigma_{AHT_{\Phi_{\max}}}} \right. \\
 &\quad + \Gamma(OHT_{\Phi_{\max}}, SW_{sfc}) \times \frac{\sigma_{SW_{sfc}}}{\sigma_{AHT_{\Phi_{\max}}}} + \Gamma(OHT_{\Phi_{\max}}, LW_{TOA}) \\
 &\quad \times \frac{\sigma_{LW_{TOA}}}{\sigma_{AHT_{\Phi_{\max}}}} + \Gamma(OHT_{\Phi_{\max}}, LW_{sfc}) \times \frac{\sigma_{LW_{sfc}}}{\sigma_{AHT_{\Phi_{\max}}}} \\
 &\quad + \Gamma(OHT_{\Phi_{\max}}, LHF_{sfc}) \times \frac{\sigma_{LHF_{sfc}}}{\sigma_{AHT_{\Phi_{\max}}}} \\
 &\quad \left. + \Gamma(OHT_{\Phi_{\max}}, SHF_{sfc}) \times \frac{\sigma_{SHF_{sfc}}}{\sigma_{AHT_{\Phi_{\max}}}} \right] \frac{\sigma_{AHT_{\Phi_{\max}}}}{\sigma_{OHT_{\Phi_{\max}}}}. \quad (9)
 \end{aligned}$$

The regression ( $C_R$ ) decomposition using each subcomponent of AHT in Eq. (9) for every CMIP6 piControl simulation considered here, along with the multimodel mean and its interquartile range, is presented in the form of bar plots in Figs. 3 and 4. The individual panels are organized by decreasing levels of NH BJC anticorrelation going left to right and top to bottom. In each panel, the first bar (dark blue) shows the total OHT – AHT regression at the latitude of maximum NH BJC [lhs in Eq. (9)]. The bars to the right of the vertical line represent the total net shortwave (gray), total net longwave (light green), and total turbulent flux (turquoise) contributions to BJC (sum of first, middle, and last two terms in the rhs of Eq. (9), respectively). The bars to the left of the vertical line represent these same terms separated into their surface and TOA contributions [single terms in rhs of Eq. (9)].

This decomposition indicates that BJC in the NH high latitudes is connected with an imbalance between net turbulent and total net longwave fluxes. A physical interpretation of the results presented in the bar plot is shown in the schematic in Fig. 5. For all models, during positive anomalous  $OHT_{\Phi_{\max}}$ , the turbulent fluxes (turquoise bar) contribute directly to the atmospheric heat gain via latent and sensible heat exchanges at the ocean surface. The light green bar indicates that the atmospheric heat gained from turbulent fluxes is accompanied by a net loss of heat from the atmosphere via longwave radiation [more heat is lost at the TOA (red) than gained from the surface (purple)]. The total net shortwave flux contribution to BJC (gray bar) is minimal because the surface and TOA counterparts (orange and dark green bars) nearly cancel each other. This behavior can be slightly different for different CMIP6 simulations, but the multimodel mean confirms that, on average, BJC in the NH high latitudes over decadal to longer time scales is mainly explained by the surface turbulent fluxes, with an important modulation mechanism provided by the total longwave radiation fluxes.

#### d. Regression maps between OHT and processes contributing to AHT

Physical features, processes, and geographic regions influencing NH BJC can be exposed by evaluating the spatial distribution of regressions of the surface and TOA fluxes and other fields that could influence Arctic oceanic and atmospheric heat content, and (eventually) OHT and AHT. We demonstrate this by focusing on the CMIP6 model that has the highest BJC anticorrelation (CNRM-CERFACS:CNRM-ESM2-1), displaying regressions of anomalous  $OHT_{65^{\circ}\text{N}}$  with detrended anomalies (smoothed using a 10-yr running mean) of various fields in Figs. 6–10 (see section 2). Our choice for the sign convention for heat/energy fluxes is such that a positive energy flux contributes to an atmospheric heat gain. At the surface that heat gain comes at the expense of the ocean heat loss. At the TOA the heat gain is associated with extra absorption of sunlight, or reduced emission of longwave radiation to space.

Figure 6 shows normalized regression maps of surface fluxes (latent, sensible, net shortwave, and net longwave radiation in Figs. 6a–d, respectively) onto  $OHT_{65^{\circ}\text{N}}$ . The high-latitude regions (north of  $65^{\circ}\text{N}$ ) that exhibit robust and consistent exchange of fluxes are the Greenland, Iceland, and the Barents Seas. Strong and consistent responses are found here due to the intense air-sea interactions. Normalized regression maps of surface ocean temperature onto  $OHT_{65^{\circ}\text{N}}$  confirm a rise in ocean temperature over the Greenland, Iceland and Barents Seas during positive  $OHT_{65^{\circ}\text{N}}$  (not shown). The atmosphere gains heat from positive  $OHT_{65^{\circ}\text{N}}$  anomalies through surface latent (Fig. 6a) and sensible (Fig. 6b) heat fluxes in the Greenland, Iceland, and Barents Seas. The surface shortwave energy flux (Fig. 6c) is a source of heat to the ocean in these regions when poleward  $OHT_{65^{\circ}\text{N}}$  anomalies occur. Our hypothesis here is that this is linked to changes in surface albedo, which in turn are associated with sea ice changes. Indeed, regression maps of sea ice concentration

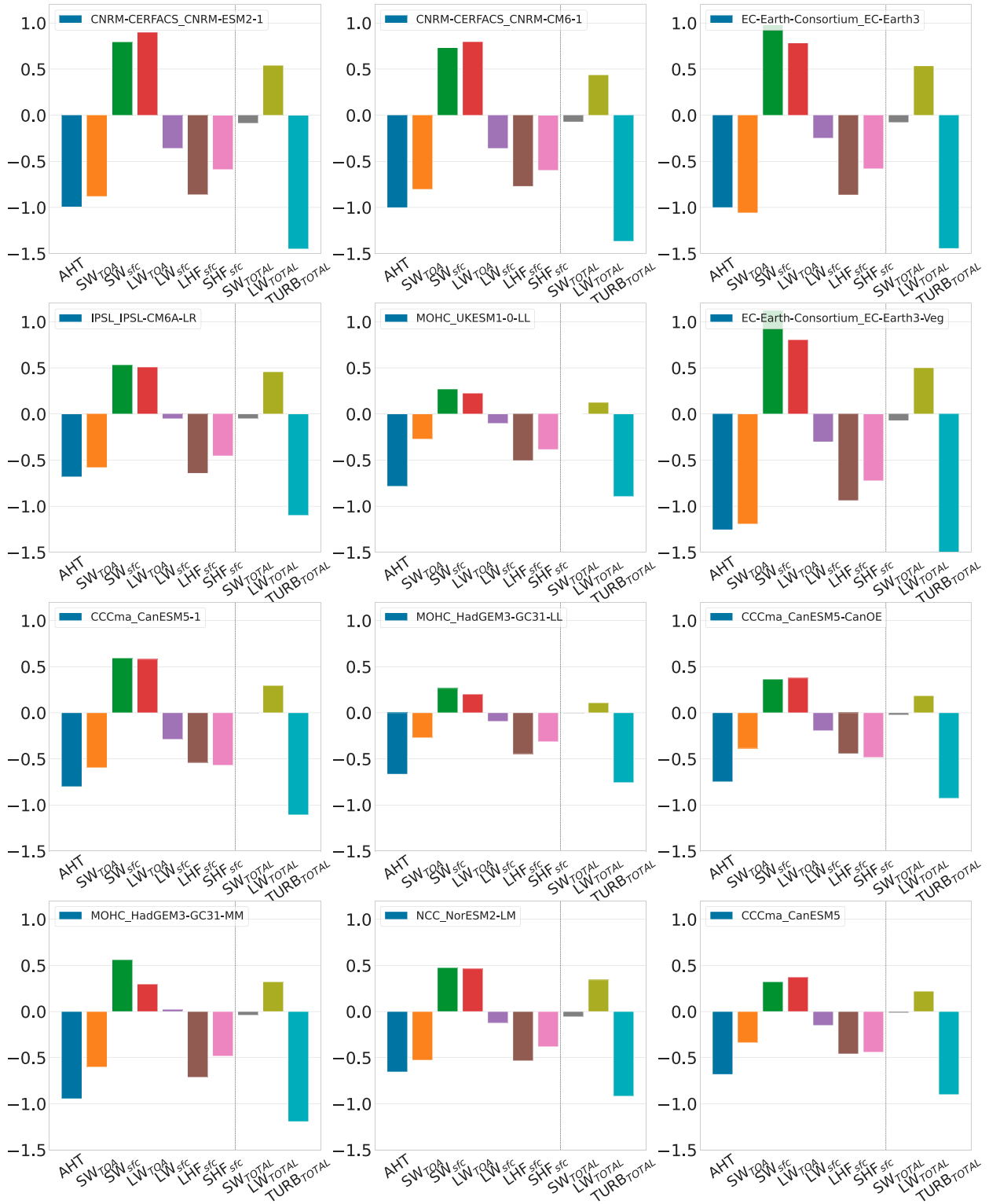


FIG. 3. Decomposition of the regression between  $OHT_{\Phi_{max}}$  and  $AHT_{\Phi_{max}}$  for 12 CMIP6 piControl models. Each bar represents a term in Eq. (9) consisting of the regression between a surface or TOA flux and OHT.

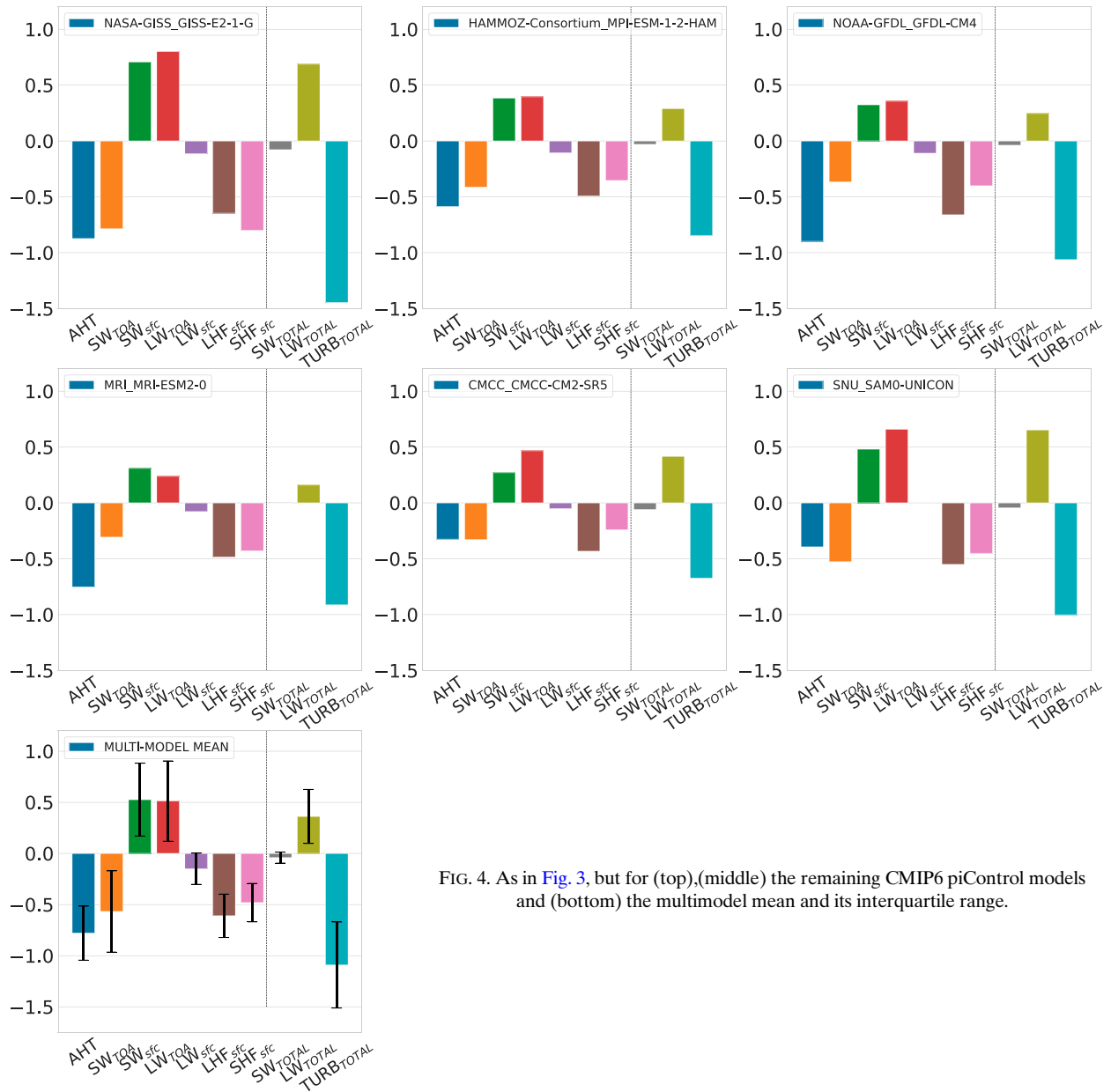


FIG. 4. As in Fig. 3, but for (top),(middle) the remaining CMIP6 piControl models and (bottom) the multimodel mean and its interquartile range.

onto OHT<sub>65°N</sub> (Fig. 7) are consistent with the patterns in Fig. 6c. This suggests that a loss of sea ice resulting from increased OHT into the Greenland, Iceland, and Barents Seas causes a reduction in surface albedo and an increase in surface shortwave radiation into the ocean. Since sea ice also serves as an insulator, its loss also supports increased longwave heat loss from the warmer ocean (Fig. 6d). The North Atlantic also shows a strong regression between OHT<sub>65°N</sub> and surface latent heat flux (Fig. 6a) but its signature is generally weaker than that coming from sensible heat fluxes.

The oversized role of sea ice in the context of NH BJC through its influence on the surface energy budget is evident from this analysis. However, the presence of clouds is another

critical factor that impacts the surface energy budget through radiative fluxes at the surface and TOA. Clouds influence the surface and TOA radiative fluxes in two opposing ways, warming the surface below them by trapping longwave radiation and cooling the region above by reflecting shortwave radiation. It is useful to understand clear-sky impacts first in order to estimate the effects of clouds at the surface and TOA in polar regions. We, therefore, investigate the importance of clear sky and clouds in the following two sections.

#### e. Sea ice and cloud radiative contributions breakdown

This section describes the role of sea ice and cloud on the radiative fluxes that are important for BJC. The approach

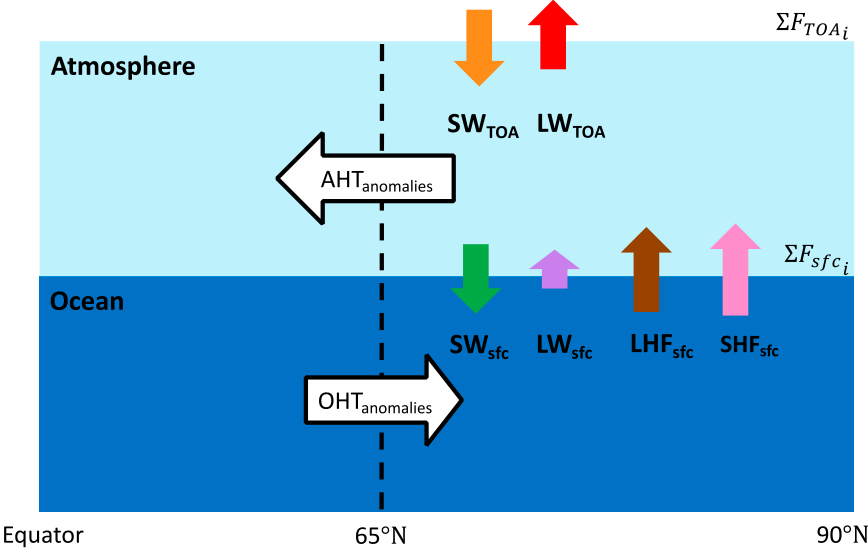


FIG. 5. Schematic of the different subcomponents of the OHT–AHT regression in Figs. 3 and 4 in and out of the ocean and atmosphere.

here is to break down the all-sky net radiative fluxes at the TOA and at the surface into shortwave and longwave components, and then further decompose each broadband flux into contributions associated with the cloud radiative effect (CRE) and the clear-sky fluxes that are very sensitive to sea ice changes, as outlined in section 2c. The sign convention for our flux definitions has been chosen so that a positive flux operating by itself indicates a warming in the atmospheric column. The fluxes are defined in terms of the CMIP6 standard variables (see Table 2 for a more detailed explanation of each flux). To expose how sea ice and clouds modulate the response of AHT to anomalous poleward OHT<sub>65°N</sub>, we calculate the four terms in Eqs. (4) and (5) separately and regress each with OHT<sub>65°N</sub>, focusing again on the simulation with the highest BJC, i.e., CNRM-CERFACS:CNRM-ESM2-1.

Regression maps for the terms in Eq. (4) (longwave radiation fluxes) are presented in Fig. 8 for the surface, TOA, and net atmosphere (surface + TOA) contributions in the first, second, and third column, respectively, and the clear-sky, cloudy, and all-sky contributions are shown in the first, second, and third row, respectively. Positive values indicate regions in the atmosphere where there is an increase in the terms in Eq. (4) (i.e., energy gains from the atmosphere perspective). Each panel also indicates the area-weighted regression coefficient integrated poleward from 65°N, therefore quantifying the effect of the individual terms in Eq. (4).

The atmosphere gains longwave radiation from the ocean surface in response to positive OHT<sub>65°N</sub> in clear-sky conditions (Fig. 8a), particularly in the Greenland, Iceland, and Barents Seas, and loses it to space at the TOA (Fig. 8b). The net effect for the atmosphere column (Fig. 8c) is a heat loss due to clear-sky longwave effects everywhere except for the Greenland, Iceland, and Barents Seas. The integrated

regression coefficients in the lower right corner of Fig. 8c quantify this effect. While the atmosphere gains longwave radiation from a generally warmer ocean, the associated atmospheric warming and that associated with turbulent heat exchange produces a much stronger longwave clear-sky radiation loss at TOA. In cloudy conditions, the net surface longwave flux into the atmosphere is negative poleward of 65°N over the Greenland, Iceland, and Barents Seas and positive over the Norwegian Sea (Fig. 8d). The dipole pattern in the Nordic seas can be attributed to changes in clouds, as described in more detail in section 3f.

The regression maps for the terms in Eq. (5) (shortwave radiation fluxes) are presented in Fig. 9. In clear-sky conditions, shortwave radiation gained by the atmosphere at TOA (Fig. 9b) is almost completely balanced by the loss of shortwave radiation to the surface (Fig. 9a) that comes from decreased albedo associated with a warmer ocean with less sea ice. As a result, there is little impact on the atmosphere column net shortwave budget (Fig. 9c).

Clouds tend to counter the clear-sky impact over marginal ice regions, shield the atmosphere from incoming energy at the TOA (Fig. 9e), and transmit less energy to the ocean in those regions (Fig. 9d), also with little net impact on the atmosphere column (Fig. 9f). The clear-sky radiative flux anomalies are substantially larger than the cloud response and dominate the all-sky flux anomalies poleward of 65°N over ice, whereas the clouds contribution dominates the all-sky flux anomalies over the central North Atlantic (Figs. 9g–i). Similar signatures (Figs. 8 and 9) exist in other simulations as well.

To better understand the cloud response patterns in Figs. 8d–f and 9d–f, we need to connect them to the presence or absence of clouds. We consider how the cloud radiative response is related to the cloud water path, a

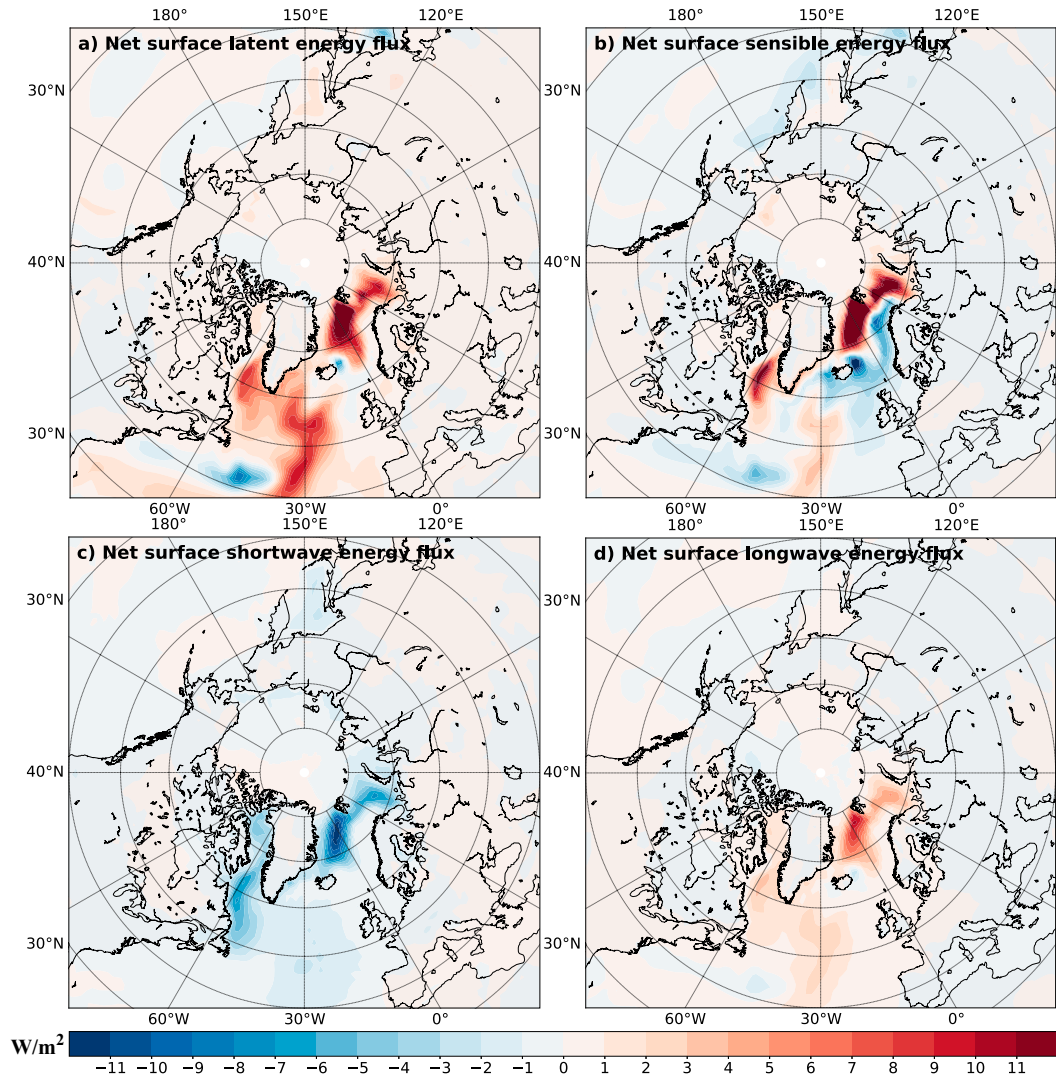


FIG. 6. Regression maps of the components that contribute to the net surface energy flux on the OHT<sub>65°N</sub> for the simulation with the highest BJC (CNRM-CERFACS:CNRM-ESM2-1). The positive values in the regression maps indicate energy flow into the atmosphere. These regression coefficients have been normalized by the standard deviation of OHT<sub>65°N</sub>.

fundamental physical property of clouds, in the following section.

#### *f. The response of clouds to increased poleward OHT<sub>65°N</sub>*

The total water path (TWP) is the amount of condensed water present in an atmospheric column per unit surface area and is an important property of clouds. The regression map of the cloud TWP [liquid water (LWP) + ice water path (IWP)] regressed against the poleward OHT<sub>65°N</sub> is shown in Fig. 10 for the CNRM-CERFACS:CNRM-ESM2-1 simulation. During periods of increased poleward OHT<sub>65°N</sub>, TWP is found to increase over the Greenland, Iceland, and Barents Seas and decrease over the Norwegian Sea.

These regional patterns in the cloud TWP response are consistent with those of longwave fluxes at TOA and surface

(Figs. 8d,e). The longwave energy loss is smaller in cloudy regions at the TOA producing a net atmospheric gain over the Greenland, Iceland, and Barents Seas (Fig. 8e). The cloud impact on the heating of the atmospheric column over the whole Arctic from longwave radiation (Fig. 8e) is small as quantified by the integrated regression coefficient in Fig. 8f. The net surface (Fig. 8g) and TOA (Fig. 8h) response is dominated by the clear-sky fluxes. There is an impact from increased clouds seen at the TOA coupled with sea ice decreases that leads to a reduction of the longwave energy loss from the ocean (Fig. 8d).

The cloud TWP response to the ocean heating anomaly is also consistent with the signatures in shortwave fluxes at TOA and surface (Figs. 9d,e). LWP increases are directly connected to albedo change, which in turn influences the TOA

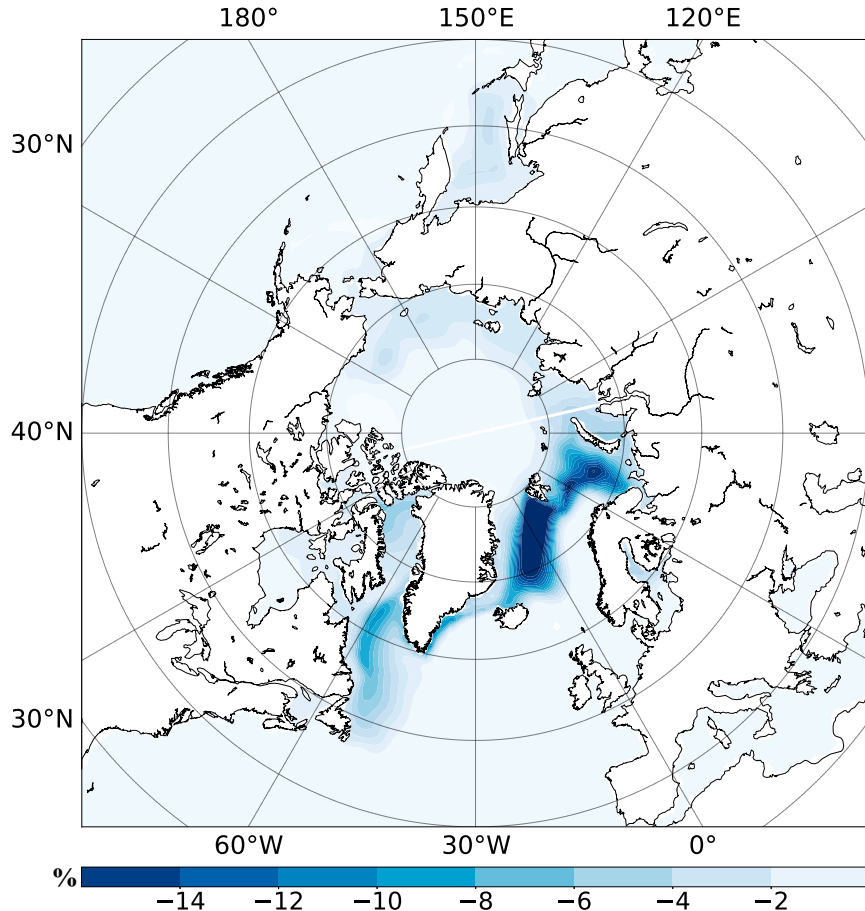


FIG. 7. Regression map of sea ice fraction on the  $OHT_{65^{\circ}\text{N}}$  for the simulation with the highest BJC (CNRM-CERFACS:CNRM-ESM2-1). The negative values in the regression maps indicate a loss of sea ice. Regression coefficients have been normalized by the standard deviation of  $OHT_{65^{\circ}\text{N}}$ .

flux (Fig. 9e). The increase in cloud TWP follows positive poleward  $OHT_{65^{\circ}\text{N}}$  (positive values in Fig. 10) and leads to an increase in cloud albedo than in turn decreases the TOA incoming shortwave radiation (negative values in Fig. 9e). The story is more complex at the surface (Fig. 9d); regions experiencing an increase in net shortwave radiation (Fig. 9d), namely, the Greenland, Iceland, and Barents Seas, during periods of positive poleward  $OHT_{65^{\circ}\text{N}}$ , also see an increase in the cloud TWP (Fig. 10). The isotropic single layer model analysis of Donohoe et al. (2020) shows (as illustrated in their Fig. 3) that in the presence of sea ice, the net shortwave radiation balance at the surface is the result of multiple reflections between the surface and cloud base and for certain values of sea ice and cloud albedo, there can still be an increase in the net shortwave radiation at the surface into the atmosphere due to increase in clouds despite the sea ice loss that follows periods of poleward  $OHT_{65^{\circ}\text{N}}$ . On the other hand, regions such as the Norwegian Sea with a negative surface shortwave radiation effect in Fig. 9d are associated with a decrease in the cloud TWP in Fig. 10, and this can be explained by a

decreased cloud albedo that allows more shortwave radiation to reach the ocean surface.

#### 4. Discussion

Our analysis indicates that the modulating effects of sea ice are robust across many CMIP6 simulations considered in this paper. Figures 11 and 12 show regression maps of sea ice concentration anomalies on normalized  $OHT_{65^{\circ}\text{N}}$  from 16 of the 18 CMIP6 simulations analyzed in section 3c (similar to Fig. 7; note that two simulations, CNRM-CERFACS:CNRM-CM6-1 and NASA-GISS:GISS-E2-1-G, were excluded due to lack of sea ice concentration data). The maps are arranged by decreasing levels of NH BJC going from left to right and top to bottom, with the area-weighted regression coefficients indicated at the bottom right corner of each panel (note that the regression coefficients are integrated poleward from  $65^{\circ}\text{N}$ ).

The magnitude of the regression coefficients indicates that simulations with the most significant sea ice loss per standard

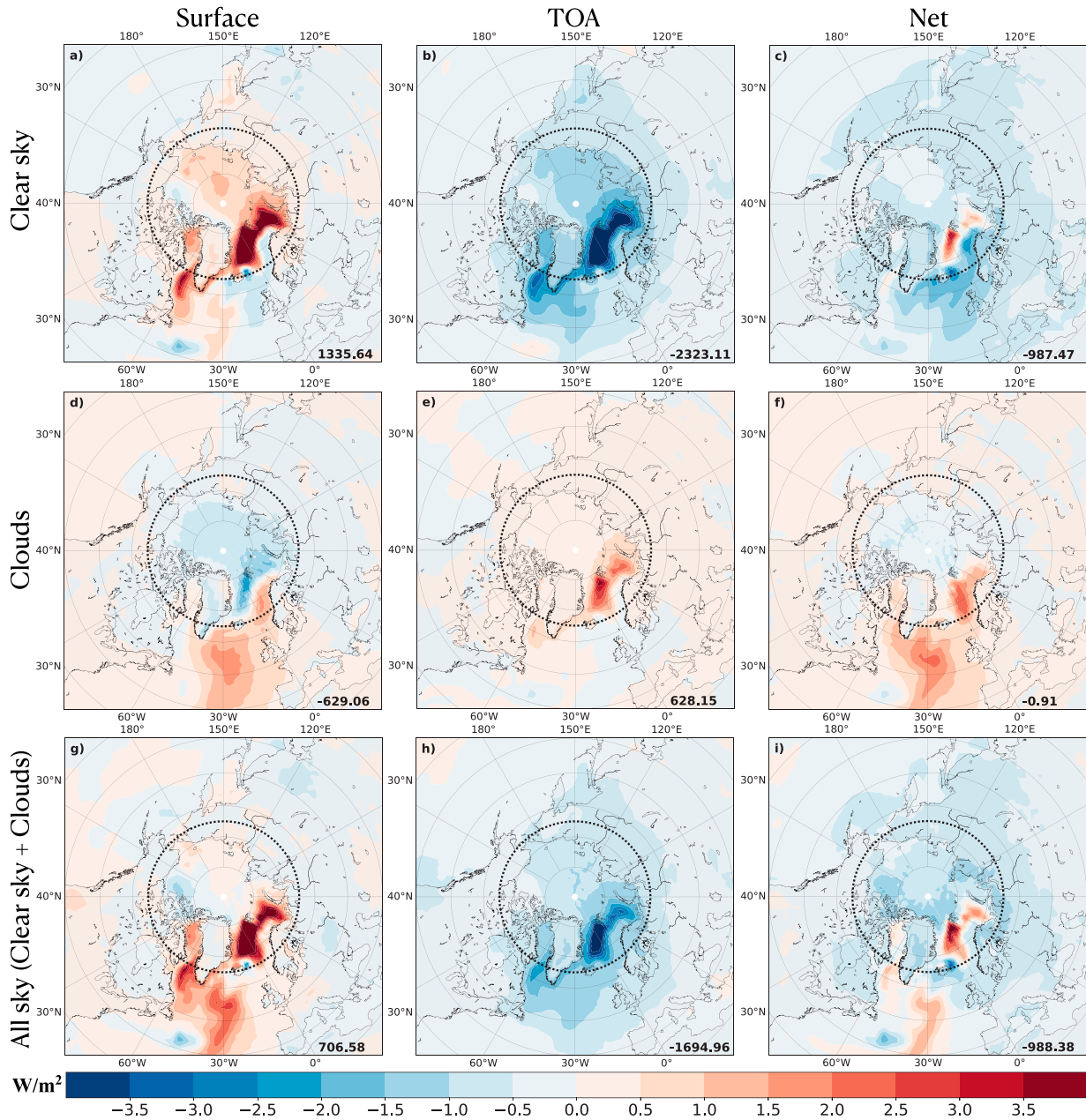


FIG. 8. Regressions maps of OHT<sub>65°N</sub> on the longwave terms in Eq. (4) for the simulation with the highest BJC (CNRM-CERFACS:CNRM-ESM2-1). (a)–(c) Maps of clear-sky surface, TOA, and net LW fluxes ( $LW_{\text{clear-sky}}^{\text{fc}}$ ,  $LW_{\text{clear-sky}}^{\text{TOA}}$ , and  $LW_{\text{clear-sky}}^{\text{net}}$ , respectively). (d)–(f) Regression maps for the cloud contribution ( $LW_{\text{clouds}}^{\text{fc}}$ ,  $LW_{\text{clouds}}^{\text{TOA}}$ , and  $LW_{\text{clouds}}^{\text{net}}$ , respectively), (g)–(i) Regression maps for the all-sky ( $LW_{\text{all-sky}}^{\text{fc}}$ ,  $LW_{\text{all-sky}}^{\text{TOA}}$ , and  $LW_{\text{all-sky}}^{\text{net}}$ , respectively). The regression coefficients integrated poleward of 65°N (area inside dashed circle) and weighted by the cell area are also presented for each regression map (number in lower-right corner in each panel) so that the net effect on the polar region north of 65°N can be clearly quantified as a net gain or loss for the Arctic atmosphere.

deviation change of anomalous OHT<sub>65°N</sub> have the strongest BJC. As previously established, the Greenland, Iceland, and Barents Seas experience the most significant sea ice loss, and this is primarily associated with an exchange of turbulent fluxes (regression maps for the turbulent fluxes are not shown; integrated results can be seen in Figs. 3 and 4. These conclusions are consistent with studies

that explore sea ice response to anomalous OHT (Aylmer et al. 2022; Nummelin et al. 2017), which find that sea ice extent is anticorrelated with poleward OHT primarily due to ocean heat convergence along the NH sea ice edge leading to sea ice loss.

By comparing the simulations with highest and lowest BJC (CNRM-CERFACS:CNRM-ESM2-1 and SNU:SAM0-UNICON,

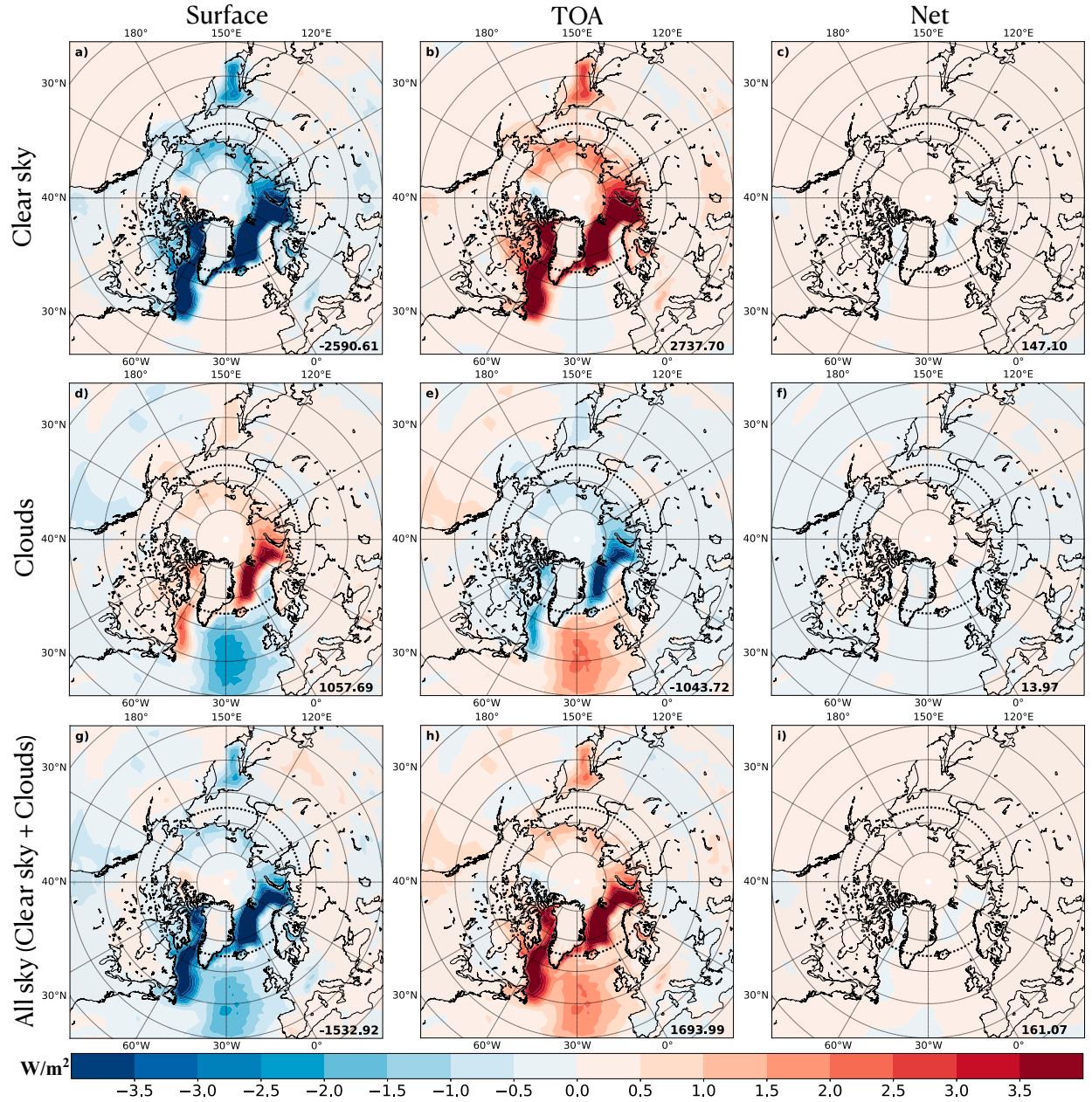


FIG. 9. As in Fig. 8, but for the corresponding shortwave terms in Eq. (5).

respectively), one can draw two inferences. First, the level of BJC present in a simulation is heavily influenced by the sensitivity of the sea ice to poleward OHT<sub>65°N</sub>. Second, the processes responsible for NH BJC primarily occur over the marginal ice zones. These results are further summarized in Fig. 13a, which shows a scatterplot of the area-weighted regression coefficients (also presented in Fig. 11) against the correlation between OHT and AHT at  $\Phi_{\max}$ . The correlation is 0.73, with a  $p$  value of 0.001 (the Pearson correlation between two time series is considered significant at the 95% significance level if the  $p$  value is less than 0.05). This further demonstrates the strong

impact of processes occurring in the Greenland, Iceland, and Barents Seas on NH BJC.

The impact of clouds in terms of TWP on NH BJC for all CMIP6 simulations is summarized in Fig. 13b. Furthermore, we present regression maps of turbulent fluxes, TWP, longwave and shortwave fluxes onto OHT<sub>65°N</sub> for the simulation with the lowest BJC (SNU:SAM0-UNICON) in Figs. S1–S4 in the online supplemental material, respectively. Comparing Fig. 10 with Fig. S2, we note an increase in TWP over the marginal ice zones in both the highest-BJC and lowest-BJC simulations during anomalous poleward OHT<sub>65°N</sub>. However, the increase in

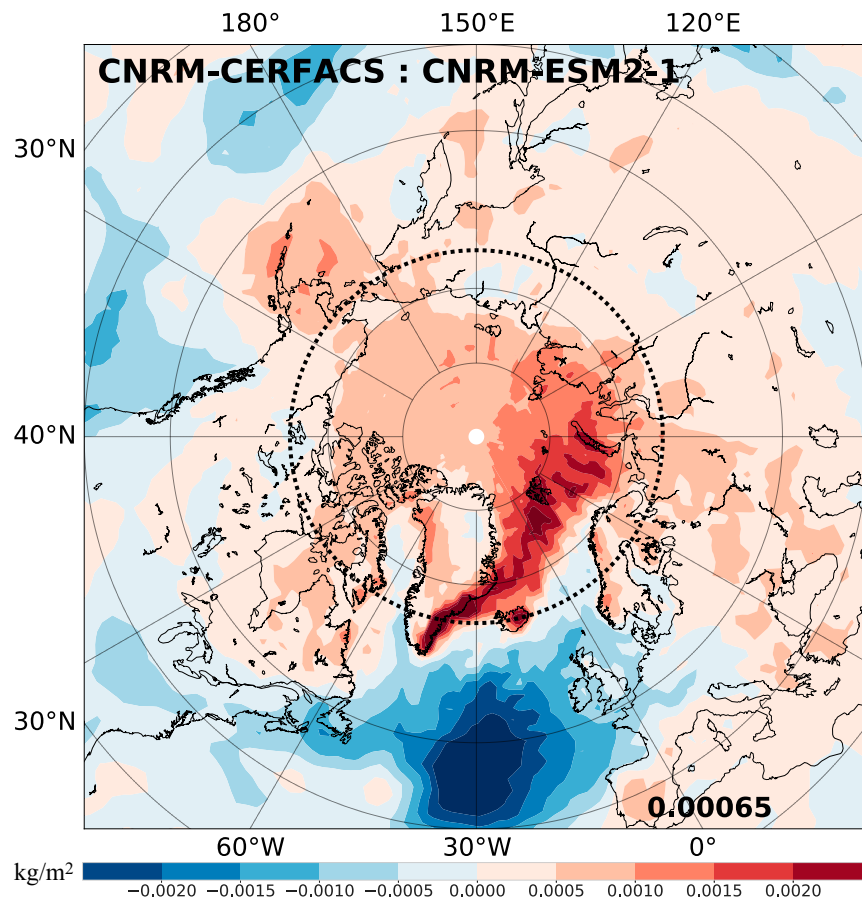


FIG. 10. Regression map of cloud total water path (TWP) on the OHT<sub>65°N</sub> for the simulation with the highest BJC (CNRM-CERFACS:CNRM-ESM2-1). Negative values indicate a reduction in TWP. Regression coefficients have been normalized by the standard deviation of OHT<sub>65°N</sub>. The poleward-integrated area-weighted regression coefficient is also shown in the lower-right corner.

TWP in the highest-BJC simulation is more than 3 times larger than that for the lowest-BJC simulation. While this relationship may appear very strong when looking at these two simulations, it becomes weaker when all the simulations in the piControl experiment are considered (Fig. 13b). The correlation between the area-weighted regression coefficient of the TWP and the BJC is  $-0.56$ , with a  $p$  value of  $0.046$ . While this correlation is still significant, the scatter in Fig. 13b suggests that the cloud response to poleward OHT<sub>65°N</sub> is also dependent on processes other than those measured by the correlation between OHT and AHT at  $65^{\circ}\text{N}$ , and thus, the relationship is weaker than that seen in Fig. 13a.

Comparing Fig. 8 with Fig. S3, we note that the lowest-BJC simulation has a significantly weakened clear-sky response at the surface (Fig. 8a, Fig. S3a). The atmosphere gains heat from the ocean via longwave radiative fluxes (Fig. S3a) in response to OHT variations, particularly over the regions associated with sea ice loss (Fig. 11: SNU:SAM0-UNICON). Heat loss at the TOA (Fig. S3b) exceeds surface gain under clear-sky conditions, although the loss is more significant in the highest-BJC simulation (Fig. 8b). This atmospheric longwave

cooling is consistent across all the simulations in the piControl simulations as shown by the light green bar plot in Fig. 4 (multimodel mean panel).

## 5. Conclusions

BJC is of great importance to the climate system, as it reflects the planet's ability to dampen polar warming during periods of increased OHT. Understanding the factors that contribute to BJC is critical for assessing the representation of BJC in climate models. The primary goal of this study is to understand factors influencing the natural variability of BJC and the role of sea ice and clouds in mediating energy transports in the ocean and atmosphere. To this end, we investigated the causes of the intermodel spread of BJC in preindustrial control simulation of the CMIP6 ensemble. In particular, we analyzed the response of the Arctic climate system to variability in the meridional OHT across  $65^{\circ}\text{N}$ . We devised a novel way to quantify the contributions from different energy exchange processes to atmospheric meridional heat transport.

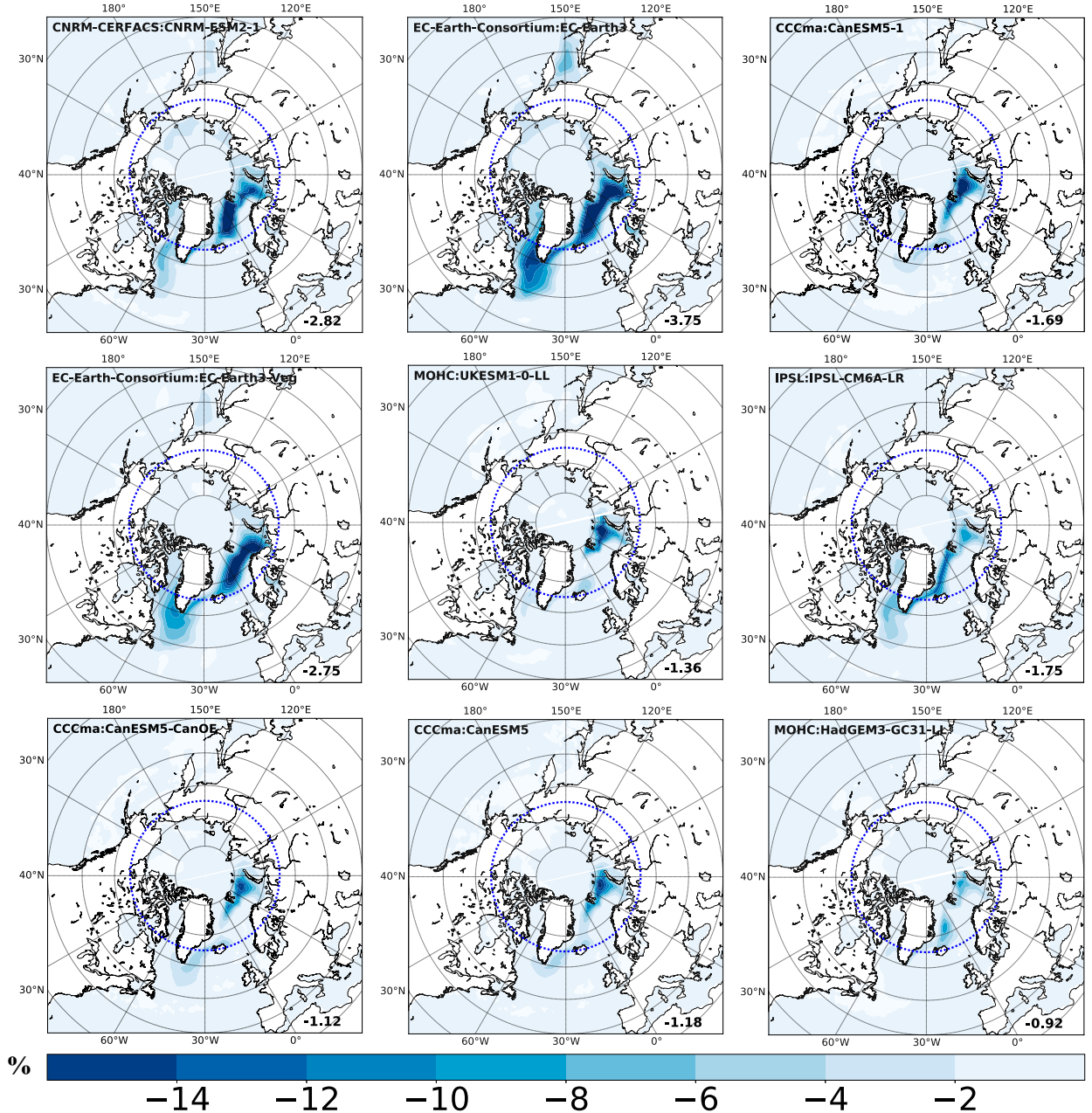


FIG. 11. Regression maps of sea ice concentration on the  $OHT_{65^{\circ}N}$  across nine CMIP6 simulations in the preindustrial control experiment. The regression coefficients in each map have been normalized by the standard deviation of the  $OHT_{65^{\circ}N}$ . The panels are arranged with the simulations organized by decreasing levels of BJC going left to right and top to bottom. The poleward-integrated area-weighted regression coefficient is also shown in the lower-right corner of each panel.

Our findings show that under natural variability, BJC is primarily driven by turbulent heat exchanges through latent and sensible heat fluxes across the air-sea interface. Increasing poleward OHT would warm the upper ocean, increasing atmospheric fluxes through surface longwave, latent heat, and sensible heat fluxes. The warm ocean results in sea ice loss, leading to an increase in downward (absorbed) surface shortwave radiation by the darker

surface. Increased water vapor from the surface and changes in atmospheric stability impact clouds and surface/TOA radiative fluxes. If the TOA/surface flux changes acted to warm the Arctic atmosphere, the pole-to-equator temperature gradient would be reduced, with a likely reduction in poleward AHT, enhancing BJC. If TOA/surface flux changes led to cooling, the pole-to-equator temperature gradient would increase and drive a stronger poleward

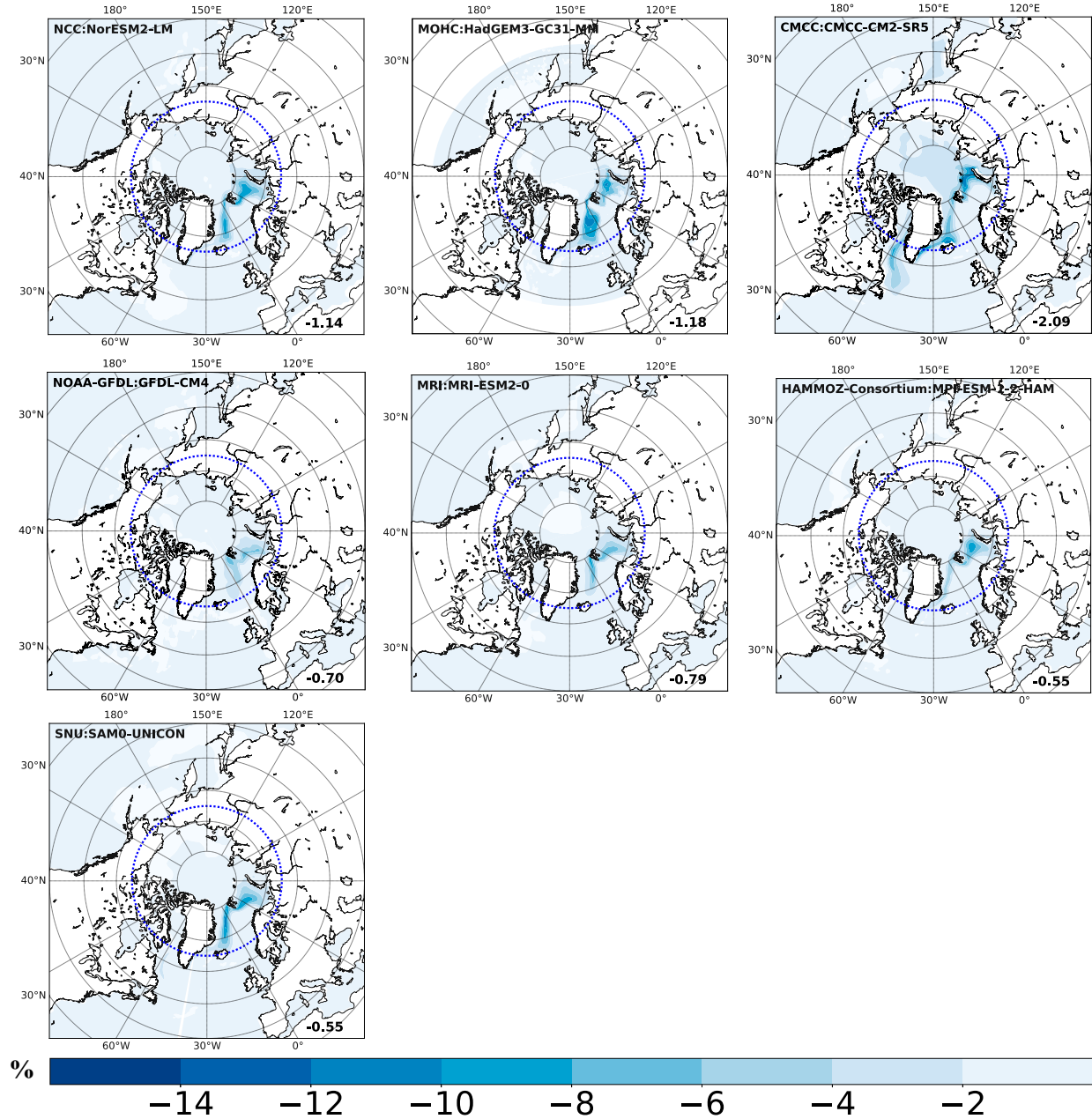


FIG. 12. As in Fig. 11, but for seven other CMIP6 simulations.

AHT, opposing BJC. The strength of the BJC is thus strongly influenced by the relative changes in the clouds, water vapor, and sea ice, each radiatively crucial in influencing the longwave and shortwave fluxes. BJC is strongest in models that have the largest sensitivity of sea ice to poleward OHT, as the positive ice-albedo feedback contributes strongly to the atmospheric response. The impact of clouds, on the other hand, is relatively small, but tends to oppose the ice-albedo feedback. Analysis using CMIP6 models and observations reveal that the Arctic warming is 4 times higher than the global

mean between October and December (Rantanen et al. 2022). Future studies on CMIP6 simulations in the historical (varying greenhouse gas forcing following the recent historical pattern), 1pctCO<sub>2</sub> experiments (with a 1% per year increase in CO<sub>2</sub>), and abrupt-4 × CO<sub>2</sub> (CO<sub>2</sub> is abruptly quadrupled and then held constant for 150 years) experiments could examine the role of the sea ice and cloud processes to see how BJC changes in a warmer climate. This study suggests that in the future an ice-free Arctic might produce significantly different BJC interactions governing AHT

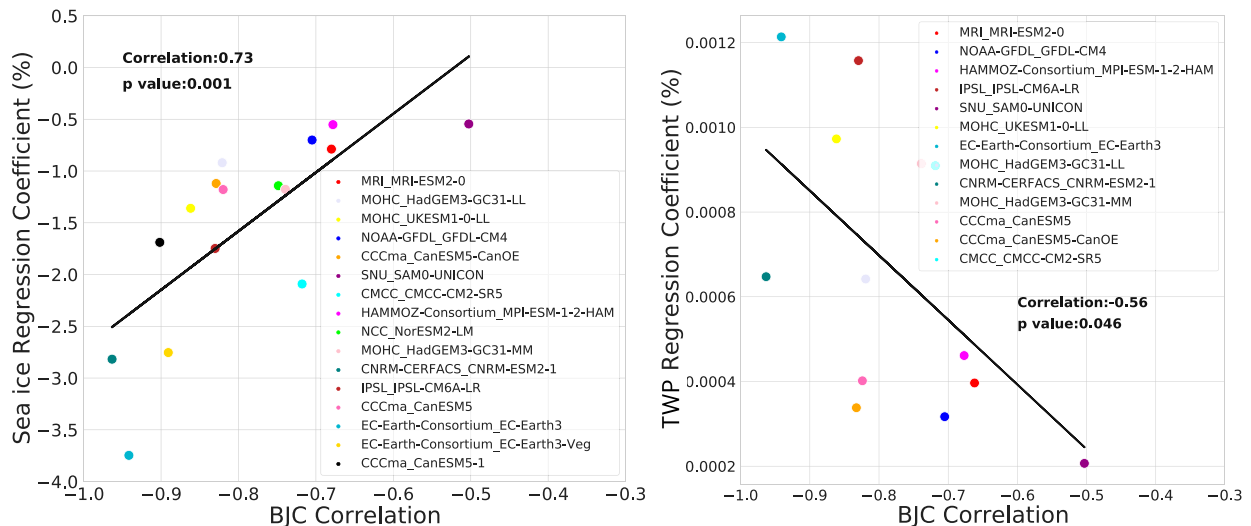


FIG. 13. Scatterplot of the poleward integrated regression coefficients of (a) sea ice concentration (numbers in lower-right corners of each panel in Fig. 11) and (b) TWP, against OHT–AHT correlation at  $\Phi_{\max}$  for all simulations in the preindustrial control experiment.

and OHT due to the sea ice and cloud radiative feedbacks discussed in this study.

**Acknowledgments.** This research was supported by the Regional and Global Model Analysis (RGMA) component of the Earth and Environmental System Modeling (ESMD) program of the U.S. DOE's Office of Science, as contribution to the HiLAT-RASM project. PK also acknowledges the support of the LANL/LDRD Program through the Center for Nonlinear Studies. The analysis of this paper were performed at the National Energy Research Scientific Computing Center (NERSC), a U.S. DOE's Office of Science User Facility operated under Contract DE-AC02-05CH11231. We acknowledge the World Climate Research Programme for coordinating CMIP6. We thank the climate modeling groups for producing and distributing their model output and the Earth System Grid Federation (ESGF) for storing and providing access to the data.

**Data availability statement.** The CMIP6 data utilized in this paper are publicly available on the ESGF data server (<https://esgf-node.llnl.gov/projects/cmip6/>).

## REFERENCES

- Alkama, R., P. C. Taylor, L. Garcia-San Martin, H. Douville, G. Duveiller, G. Forzieri, D. Swingedouw, and A. Cescatti, 2020: Clouds damp the radiative impacts of polar sea ice loss. *Cryosphere*, **14**, 2673–2686, <https://doi.org/10.5194/tc-14-2673-2020>.
- Aylmer, J., D. Ferreira, and D. Feltham, 2022: Different mechanisms of Arctic and Antarctic sea ice response to ocean heat transport. *Climate Dyn.*, **59**, 315–329, <https://doi.org/10.1007/s00382-021-06131-x>.
- Bjerknes, J., 1964: Atlantic air-sea interaction. *Advances in Geophysics*, Vol. 10, Academic Press, 1–82, [https://doi.org/10.1016/S0065-2687\(08\)60005-9](https://doi.org/10.1016/S0065-2687(08)60005-9).
- Boucher, O., and Coauthors, 2018: IPSL IPSL-CM6A-LR model output prepared for CMIP6 CMIP piControl. Earth System Grid Federation, accessed 15 November 2021, <https://doi.org/10.22033/ESGF/CMIP6.5251>.
- Budyko, M. I., 1969: The effect of solar radiation variations on the climate of the Earth. *Tellus*, **21A**, 611, <https://doi.org/10.3402/tellusa.v21i5.10109>.
- Cheng, L., and Coauthors, 2022: Past and future ocean warming. *Nat. Rev. Earth Environ.*, **3**, 776–794, <https://doi.org/10.1038/s43017-022-00345-1>.
- Cherchi, A., and Coauthors, 2019: Global mean climate and main patterns of variability in the CMCC-CM2 coupled model. *J. Adv. Model. Earth Syst.*, **11**, 185–209, <https://doi.org/10.1029/2018MS001369>.
- Christian, J. R., and Coauthors, 2022: Ocean biogeochemistry in the Canadian Earth system model version 5.0.3: CanESM5 and CanESM5-CanOE. *Geosci. Model Dev.*, **15**, 4393–4424, <https://doi.org/10.5194/gmd-15-4393-2022>.
- Czaja, A., and J. Marshall, 2006: The partitioning of poleward heat transport between the atmosphere and ocean. *J. Atmos. Sci.*, **63**, 1498–1511, <https://doi.org/10.1175/JAS3695.1>.
- Dai, H., H. Yang, and J. Yin, 2017: Roles of energy conservation and climate feedback in Bjerknes compensation: A coupled modeling study. *Climate Dyn.*, **49**, 1513–1529, <https://doi.org/10.1007/s00382-016-3386-y>.
- Donohoe, A., E. Blanchard-Wrigglesworth, A. Schweiger, and P. J. Rasch, 2020: The effect of atmospheric transmissivity on model and observational estimates of the sea ice albedo feedback. *J. Climate*, **33**, 5743–5765, <https://doi.org/10.1175/JCLI-D-19-0674.1>.
- Döscher, R., and Coauthors, 2022: The EC-Earth3 Earth system model for the Coupled Model Intercomparison Project 6. *Geosci. Model Dev.*, **15**, 2973–3020, <https://doi.org/10.5194/gmd-15-2973-2022>.
- EC-Earth, 2019a: EC-Earth-Consortium EC-Earth3 model output prepared for CMIP6 CMIP piControl. Earth System Grid Federation, accessed 15 November 2021, <https://doi.org/10.22033/ESGF/CMIP6.4842>.

- , 2019b: EC-Earth-Consortium EC-Earth3-Veg model output prepared for CMIP6 CMIP piControl. Earth System Grid Federation, accessed 15 November 2021, <https://doi.org/10.22033/ESGF/CMIP6.4848>.
- Farneti, R., and G. K. Vallis, 2013: Meridional energy transport in the coupled atmosphere–ocean system: Compensation and partitioning. *J. Climate*, **26**, 7151–7166, <https://doi.org/10.1175/JCLI-D-12-00133.1>.
- Gosse, H., and Coauthors, 2018: Quantifying climate feedbacks in polar regions. *Nat. Commun.*, **9**, 1919, <https://doi.org/10.1038/s41467-018-04173-0>.
- Guo, H., and Coauthors, 2018: NOAA-GFDL GFDL-CM4 model output piControl. Earth System Grid Federation, accessed 22 August 2023, <https://doi.org/10.22033/ESGF/CMIP6.8666>.
- Hall, A., 2004: The role of surface albedo feedback in climate. *J. Climate*, **17**, 1550–1568, [https://doi.org/10.1175/1520-0442\(2004\)017<1550:TROSAF>2.0.CO;2](https://doi.org/10.1175/1520-0442(2004)017<1550:TROSAF>2.0.CO;2).
- Hankel, C., and E. Tziperman, 2021: The role of atmospheric feedbacks in abrupt winter Arctic sea ice loss in future warming scenarios. *J. Climate*, **34**, 4435–4447, <https://doi.org/10.1175/JCLI-D-20-0558.1>.
- Held, I. M., and Coauthors, 2019: Structure and performance of GFDL’s CM4.0 climate model. *J. Adv. Model. Earth Syst.*, **11**, 3691–3727, <https://doi.org/10.1029/2019MS001829>.
- Kelley, M., and Coauthors, 2020: GISS-E2.1: Configurations and climatology. *J. Adv. Model. Earth Syst.*, **12**, e2019MS002025, <https://doi.org/10.1029/2019MS002025>.
- Kuhlbrodt, T., and Coauthors, 2018: The low-resolution version of HadGEM3 GC3.1: Development and evaluation for global climate. *J. Adv. Model. Earth Syst.*, **10**, 2865–2888, <https://doi.org/10.1029/2018MS001370>.
- Lauer, A., L. Bock, B. Hassler, M. Schröder, and M. Stengel, 2023: Cloud climatologies from global climate models—A comparison of CMIP5 and CMIP6 models with satellite data. *J. Climate*, **36**, 281–311, <https://doi.org/10.1175/JCLI-D-22-0181.1>.
- Liu, Y., J. Attema, and W. Hazeleger, 2020: Atmosphere–ocean interactions and their footprint on heat transport variability in the Northern Hemisphere. *J. Climate*, **33**, 3691–3710, <https://doi.org/10.1175/JCLI-D-19-0570.1>.
- Lovato, T., and D. Peano, 2020: CMCC CMCC-CM2-SR5 model output prepared for CMIP6 CMIP piControl. Earth System Grid Federation, accessed 22 August 2023, <https://doi.org/10.22033/ESGF/CMIP6.3874>.
- Magnusdottir, G., and R. Saravanan, 1999: The response of atmospheric heat transport to zonally-averaged SST trends. *Tellus*, **51A**, 815, <https://doi.org/10.3402/tellusa.v51i5.14495>.
- Mauritsen, T., and Coauthors, 2019: Developments in the MPI-M Earth System Model version 1.2 (MPI-ESM1.2) and its response to increasing CO<sub>2</sub>. *J. Adv. Model. Earth Syst.*, **11**, 998–1038, <https://doi.org/10.1029/2018MS001400>.
- Mitchell, J. F., C. A. Senior, and W. J. Ingram, 1989: CO<sub>2</sub> and climate: A missing feedback? *Nature*, **341**, 132–134, <https://doi.org/10.1038/341132a0>.
- NASA-GISS, 2018: NASA-GISS GISS-E2.1G model output prepared for CMIP6 CMIP piControl. Earth System Grid Federation, accessed 22 August 2023, <https://doi.org/10.22033/ESGF/CMIP6.7380>.
- Neubauer, D., and Coauthors, 2019: HAMMOZ-Consortium MPI-ESM1.2-HAM model output prepared for CMIP6 CMIP piControl. Earth System Grid Federation, accessed 10 November 2022, <https://doi.org/10.22033/ESGF/CMIP6.5037>.
- Notz, D., and SIMIP Community, 2020: Arctic sea ice in CMIP6. *Geophys. Res. Lett.*, **47**, e2019GL086749, <https://doi.org/10.1029/2019GL086749>.
- Nummelin, A., C. Li, and P. J. Hezel, 2017: Connecting ocean heat transport changes from the midlatitudes to the Arctic Ocean. *Geophys. Res. Lett.*, **44**, 1899–1908, <https://doi.org/10.1002/2016GL071333>.
- Oldenburg, D., K. C. Armour, L. Thompson, and C. M. Bitz, 2018: Distinct mechanisms of ocean heat transport into the Arctic under internal variability and climate change. *Geophys. Res. Lett.*, **45**, 7692–7700, <https://doi.org/10.1029/2018GL078719>.
- Outten, S., I. Esau, and O. H. Otterå, 2018: Bjerknes compensation in the CMIP5 climate models. *J. Climate*, **31**, 8745–8760, <https://doi.org/10.1175/JCLI-D-18-0058.1>.
- Park, S., and J. Shin, 2019: SNU SAM0-UNICON model output prepared for CMIP6 CMIP piControl. Earth System Grid Federation, accessed 10 November 2022, <https://doi.org/10.22033/ESGF/CMIP6.7791>.
- , —, S. Kim, E. Oh, and Y. Kim, 2019: Global climate simulated by the Seoul National University Atmosphere Model version 0 with a Unified Convection Scheme (SAM0-UNICON). *J. Climate*, **32**, 2917–2949, <https://doi.org/10.1175/JCLI-D-18-0796.1>.
- Philipp, D., M. Stengel, and B. Ahrens, 2020: Analyzing the Arctic feedback mechanism between sea ice and low-level clouds using 34 years of satellite observations. *J. Climate*, **33**, 7479–7501, <https://doi.org/10.1175/JCLI-D-19-0895.1>.
- Pithan, F., and T. Mauritsen, 2014: Arctic amplification dominated by temperature feedbacks in contemporary climate models. *Nat. Geosci.*, **7**, 181–184, <https://doi.org/10.1038/ngeo2071>.
- Ramanathan, V., R. D. Cess, E. F. Harrison, P. Minnis, B. R. Barkstrom, E. Ahmad, and D. Hartmann, 1989: Cloud-radiative forcing and climate: Results from the Earth Radiation Budget Experiment. *Science*, **243**, 57–63, <https://doi.org/10.1126/science.243.4887.57>.
- Rantanen, M., A. Y. Karpechko, A. Lipponen, K. Nordling, O. Hyvärinen, K. Ruosteenoja, T. Vihma, and A. Laaksonen, 2022: The Arctic has warmed nearly four times faster than the globe since 1979. *Commun. Earth Environ.*, **3**, 168, <https://doi.org/10.1038/s43247-022-00498-3>.
- Reusen, J., E. van der Linden, and R. Bintanja, 2019: Differences between Arctic interannual and decadal variability across climate states. *J. Climate*, **32**, 6035–6050, <https://doi.org/10.1175/JCLI-D-18-0672.1>.
- Ridley, J., M. Menary, T. Kuhlbrodt, M. Andrews, and T. Andrews, 2018: MOHC HadGEM3-GC31-LL model output prepared for CMIP6 CMIP piControl. Earth System Grid Federation, accessed 15 November 2022, <https://doi.org/10.22033/ESGF/CMIP6.6294>.
- , —, —, —, and —, 2019: MOHC HadGEM3-GC31-MM model output prepared for CMIP6 CMIP piControl. Earth System Grid Federation, accessed 10 November 2022, <https://doi.org/10.22033/ESGF/CMIP6.6297>.
- Schweiger, A. J., R. W. Lindsay, S. Vavrus, and J. A. Francis, 2008: Relationships between Arctic sea ice and clouds during autumn. *J. Climate*, **21**, 4799–4810, <https://doi.org/10.1175/2008JCLI2156.1>.
- Séférian, R., 2018: CNRM-CERFACS CNRM-ESM2-1 model output prepared for CMIP6 CMIP piControl. Earth System Grid Federation, accessed 15 November 2022, <https://doi.org/10.22033/ESGF/CMIP6.4165>.
- , and Coauthors, 2019: Evaluation of CNRM earth system model, CNRM-ESM2-1: Role of Earth system processes in

- present-day and future climate. *J. Adv. Model. Earth Syst.*, **11**, 4182–4227, <https://doi.org/10.1029/2019MS001791>.
- Seland, Ø., and Coauthors, 2019: NCC NorESM2-LM model output prepared for CMIP6 CMIP piControl. Earth System Grid Federation, accessed 26 October 2021, <https://doi.org/10.22033/ESGF/CMIP6.8217>.
- , and Coauthors, 2020: Overview of the Norwegian Earth System Model (NorESM2) and key climate response of CMIP6 DECK, historical, and scenario simulations. *Geosci. Model Dev.*, **13**, 6165–6200, <https://doi.org/10.5194/gmd-13-6165-2020>.
- Sellar, A. A., and Coauthors, 2019: UKESM1: Description and evaluation of the U.K. Earth System Model. *J. Adv. Model. Earth Syst.*, **11**, 4513–4558, <https://doi.org/10.1029/2019MS001739>.
- Servonnat, J., and Coauthors, 2020: Presentation and evaluation of the IPSL-CM6A-LR climate model. *J. Adv. Model. Earth Syst.*, **12**, e2019MS002010, <https://doi.org/10.1029/2019MS002010>.
- Shaffrey, L., and R. Sutton, 2006: Bjerknes compensation and the decadal variability of the energy transports in a coupled climate model. *J. Climate*, **19**, 1167–1181, <https://doi.org/10.1175/JCLI3652.1>.
- Shi, J., and H. Yang, 2021: Bjerknes compensation in a coupled global box model. *Climate Dyn.*, **57**, 3569–3582, <https://doi.org/10.1007/s00382-021-05881-y>.
- Stapf, J., A. Ehrlich, E. Jäkel, C. Lüpkes, and M. Wendisch, 2020: Reassessment of shortwave surface cloud radiative forcing in the Arctic: Consideration of surface-albedo-cloud interactions. *Atmos. Chem. Phys.*, **20**, 9895–9914, <https://doi.org/10.5194/acp-20-9895-2020>.
- Swart, N. C., and Coauthors, 2019a: CCCma CanESM5-CanOE model output prepared for CMIP6 CMIP piControl. Earth System Grid Federation, accessed 26 October 2021, <https://doi.org/10.22033/ESGF/CMIP6.10266>.
- , and Coauthors, 2019b: CCCma CanESM5 model output prepared for CMIP6 CMIP piControl. Earth System Grid Federation, accessed 26 October 2021, <https://doi.org/10.22033/ESGF/CMIP6.3673>.
- , and Coauthors, 2019c: CCCma CanESM5.1 model output prepared for CMIP6 CMIP piControl. Earth System Grid Federation, accessed 26 October 2021, <https://doi.org/10.22033/ESGF/CMIP6.17424>.
- , and Coauthors, 2019d: The Canadian Earth System Model version 5 (CanESM5.0.3). *Geosci. Model Dev.*, **12**, 4823–4873, <https://doi.org/10.5194/gmd-12-4823-2019>.
- Tang, Y., S. Rumbold, R. Ellis, D. Kelley, J. Mulcahy, A. Sellar, J. Walton, and C. Jones, 2019: MOHC UKESM1.0-LL model output prepared for CMIP6 CMIP piControl. Earth System Grid Federation, accessed 15 November 2021, <https://doi.org/10.22033/ESGF/CMIP6.6298>.
- Trenberth, K. E., and J. M. Caron, 2001: Estimates of meridional atmosphere and ocean heat transports. *J. Climate*, **14**, 3433–3443, [https://doi.org/10.1175/1520-0442\(2001\)014<3433:EOMAAO>2.0.CO;2](https://doi.org/10.1175/1520-0442(2001)014<3433:EOMAAO>2.0.CO;2).
- , Y. Zhang, J. T. Fasullo, and L. Cheng, 2019: Observation-based estimates of global and basin ocean meridional heat transport time series. *J. Climate*, **32**, 4567–4583, <https://doi.org/10.1175/JCLI-D-18-0872.1>.
- van der Swaluw, E., S. S. Drijfhout, and W. Hazeleger, 2007: Bjerknes compensation at high northern latitudes: The ocean forcing the atmosphere. *J. Climate*, **20**, 6023–6032, <https://doi.org/10.1175/2007JCLI1562.1>.
- Voldoire, A., 2018: CMIP6 simulations of the CNRM-CERFACS based on CNRM-CM6-1 model for CMIP experiment piControl. Earth System Grid Federation, accessed 15 November 2021, <https://doi.org/10.22033/ESGF/CMIP6.4163>.
- , and Coauthors, 2019: Evaluation of CMIP6 DECK experiments with CNRM-CM6-1. *J. Adv. Model. Earth Syst.*, **11**, 2177–2213, <https://doi.org/10.1029/2019MS001683>.
- von Schuckmann, K., and Coauthors, 2016: An imperative to monitor Earth's energy imbalance. *Nat. Climate Change*, **6**, 138–144, <https://doi.org/10.1038/nclimate2876>.
- Wei, J., Z. Wang, M. Gu, J.-J. Luo, and Y. Wang, 2021: An evaluation of the Arctic clouds and surface radiative fluxes in CMIP6 models. *Acta Oceanol. Sin.*, **40**, 85–102, <https://doi.org/10.1007/s13131-021-1705-6>.
- Williams, K. D., and Coauthors, 2018: The Met Office Global Coupled model 3.0 and 3.1 (GC3.0 and GC3.1) configurations. *J. Adv. Model. Earth Syst.*, **10**, 357–380, <https://doi.org/10.1002/2017MS001115>.
- Yang, H., Y. Zhao, Z. Liu, Q. Li, F. He, and Q. Zhang, 2015: Heat transport compensation in atmosphere and ocean over the past 22,000 years. *Sci. Rep.*, **5**, 16661, <https://doi.org/10.1038/srep16661>.
- , —, and —, 2016: Understanding Bjerknes compensation in atmosphere and ocean heat transports using a coupled box model. *J. Climate*, **29**, 2145–2160, <https://doi.org/10.1175/JCLI-D-15-0281.1>.
- Yukimoto, S., and Coauthors, 2019a: MRI MRI-ESM2.0 model output prepared for CMIP6 CMIP piControl. Earth System Grid Federation, accessed 10 December 2019, <https://doi.org/10.22033/ESGF/CMIP6.6900>.
- , and Coauthors, 2019b: The Meteorological Research Institute Earth System Model version 2.0, MRI-ESM2.0: Description and basic evaluation of the physical component. *J. Meteor. Soc. Japan*, **97**, 931–965, <https://doi.org/10.2151/jmsj.2019-051>.
- Zelinka, M. D., T. A. Myers, D. T. McCoy, S. Po-Chedley, P. M. Caldwell, P. Ceppi, S. A. Klein, and K. E. Taylor, 2020: Causes of higher climate sensitivity in CMIP6 models. *Geophys. Res. Lett.*, **47**, e2019GL085782, <https://doi.org/10.1029/2019GL085782>.
- Zhao, Y., H. Yang, and Z. Liu, 2016: Assessing Bjerknes compensation for climate variability and its time-scale dependence. *J. Climate*, **29**, 5501–5512, <https://doi.org/10.1175/JCLI-D-15-0883.1>.